A global multi-scale mathematical model for the human circulation with emphasis on the venous system

L. O. Müller & E. F. Toro
Laboratory of Applied Mathematics
University of Trento
Via Mesiano 77, 38123 Trento, Italy
e-mail: lucas.mueller@ing.unitn.it, toro@ing.unitn.it

Isaac Newton Institute for Mathematical Sciences. University of Cambridge, UK.
Preprint NI13007, 2013.

4 April 2013

A global multi-scale mathematical model for the human circulation with emphasis on the venous system

L. O. Müller & E. F. Toro

Laboratory of Applied Mathematics
University of Trento
Via Mesiano 77, 38123 Trento, Italy
e-mail: lucas.mueller@ing.unitn.it, toro@ing.unitn.it

4 April 2013

Abstract

We present a global, closed-loop, multi-scale mathematical model for the human circulation including the arterial system, the venous system, the heart, the pulmonary circulation and the microcirculation. A distinctive feature of our model is the detailed description of the venous system, particularly for intra- and extra-cranial veins. Medium to large vessels are described by one-dimensional hyperbolic systems while the rest of the components are described by zero-dimensional models represented by differential algebraic equations. Robust, high-order accurate numerical methodology is implemented for solving the hyperbolic equations, which are adopted from a recent reformulation that includes variable material properties. Due to the large inter-subject variability of the venous system, we perform a patient-specific characterisation of major veins of the head and neck using MRI data. Computational results are carefully validated using published data for the arterial system and most regions of the venous system. For head and neck veins validation is carried out through a detailed comparison of simulation results against patient-specific Phase-Contrast MRI flow quantification data. A merit of our model is its global, closed-loop character; the imposition of highly artificial boundary conditions is avoided. Applications in mind include a vast range of medical conditions. Of particular interest is the study of some neurodegenerative diseases, whose venous haemodynamics connection has recently been identified by medical researchers.

1 Introduction

The present work is in part motivated by recent interest shown by the medical community on the venous system and its potential role in the development and clinical course of neurodegenerative diseases [39]. In particular, applications in mind include a theoretical study of two empirically discovered conditions, namely Chronic Cerebrospinal Venous Insufficiency [97] and Idiopathic Parkinson's Disease [40]. These motivating examples set two requirements on our model. First, the description of head and neck veins should be sufficiently detailed, including the numerous collateral pathways of cerebral venous return [73]. Second, the model should include the main systemic veins in order to take into account some specific characteristics of the pathologies under study. We have therefore chosen to construct a closed-loop model of the entire cardiovascular system with emphasis on the venous district.

In 1969, the journal IEEE Transactions on Bio-medical Engineering published an entire issue on the venous system. Main points identified by contributors included a description of mechanical properties of veins, their functioning and, consequently, their modelling. At that time the modelling community was well aware of the difficulties to be faced in order to model the venous system. The most relevant problems,

or differences, compared to the arterial counterpart, concerned the collapsibility of veins and the effect of external forces, such as gravity and external pressure, on venous flow [17]. In their introductory letter to that issue, Noordergraaf and Kresch [65] put in evidence the increasing interest in the role played by the venous system in heart dynamics and circulation in general. They concluded prospecting a renewed interest in the modelling community in this research field. Two remarkable contributions of the 1969 issue of IEEE Transactions on Bio-medical Engineering are the works by Snyder & Rideout [78] and by Moreno *et al.* [56]. Both contributions represented early attempts to model the complete cardiovascular system, giving special attention to the description of the venous district. Snyder and Rideout [78] proposed a closed-loop lumped parameter model including vessel collapse, external pressure by respiration, venous tone regulation and gravity.

Unfortunately, not much progress has been made since those early days in the field of venous haemodynamics modelling. Most of the available work concerns the description of flow in collapsible tubes [74, 45, 32] and related numerical applications to rather simple problems [71, 15, 16]. Recently, some interesting work has been published regarding the construction of tube laws for veins [10] and its application to one-dimensional modelling of blood flow in veins of the lower limb [37, 54]. Some work on modelling of venous networks with one-dimensional approaches is available in the literature. Zagzoule and MarcVergnes [96] presented a model for cerebral circulation with major arteries, intracranial veins and the jugular veins. Cirovic *et al.* [22] modelled cerebral blood flow using the network proposed in [96] and including high gravitational acceleration, observing jugular vein collapse. Sheng *et al.* [75] presented an open-loop model with a one-dimensional description of arteries, veins and capillaries. Following the work of Sheng *et al.*, Alirezaye-Davatgar [3] proposed a similar model; no emphasis on results for the venous system were given. Vassilevski *et al.* [90] proposed a closed-loop model of the cardiovascular system with a one-dimensional description of veins; no details on the construction of the venous network were provided. Finally, Ho *et al.* [42] reported the construction of a patient-specific one-dimensional model of the cerebral venous system, imposing artificial boundary conditions at the level of the superior vena cava and terminal veins.

Closed-loop models of the cardiovascular system with a one-dimensional description of major vessels are rare. Two prominent examples are the closed-loop models proposed by Liang *et al.* [51] and by Blanco *et al.* [12]. In both cases the arterial system is modelled using a one-dimensional approach, while the heart, pulmonary circulation, capillaries and veins are treated as lumped parameter compartments. We note that at the refereeing stage of this paper we were made aware of an excellent and relevant piece of work concerning a closed-loop model and one-dimensional representation of the venous system; see Mynard [62]. Our model is a step forward in the context of closed-loop models since it includes a detailed one-dimensional description of the venous district. This model will constitute the basis on which the above discussed challenges of the venous system will be approached and, hopefully, resolved.

Variation of mechanical and geometrical properties of vessels along their longitudinal axis gives rise to *geometrical-type* source terms. These source terms cause severe problems if a naive discretisation is used. We chose to adopt a reformulation of the classical equations governing one-dimensional blood flow proposed in [86], where the system is written in quasi-linear form. Concerning the numerical method for solving the one-dimensional blood flow equations in veins and arteries, we adopt the ADER framework [85]. This framework allows the construction of non-linear schemes, to circumvent Godunov's theorem, of high order of accuracy in both space and time, while maintaining the necessary robustness required by the highly non-linear behaviour of veins. High order of accuracy in space and time is mandatory; it is in fact an efficiency requirement, most relevant for the simulation of complex systems, such as the human circulation. See [57] and [59] for the case of one-dimensional blood flow models, where an analysis of convergence rates, errors and CPU time is carried out. ADER finite volume schemes consist of two building blocks: (i) a non-linear spatial reconstruction operator and (ii) the solution of the Generalized Riemann Problem (GRP) at each cell interface to compute numerical fluxes [87]. For the solution of the GRP we adopt the Dumbser-Enaux-Toro (DET) solver [28, 27, 29]. All GRP solvers available, see [55], require a classical Riemann solver. Here we use the Dumbser-Osher-Toro (DOT) Riemann solver [30], as proposed in [59]. This numerical scheme is able to treat venous collapse, as well as transcritical flows [57], which might verify in veins [77]. For background on the ADER approach and recent developments

see chapters 19 and 20 of [88] and references therein.

A distinctive aspect of this work, is the performance of a patient-specific characterization of major veins of the head and neck. This approach is motivated by the great inter-subject variability of the venous system [73, 93]. In order to achieve this goal, we represent major head and neck veins of our venous network using Magnetic Resonance Imaging derived geometrical information [89]. Moreover, we are able to compare our computational results with MRI-derived time-resolved flow quantification data [33], again, in a patient-specific manner. This is possible because MRI imaging of venous structures and flow quantification are made within the same MRI session.

The rest of the paper is structured as follows. In section 2 we present the mathematical models used to treat each compartment, whereas in section 3 we describe numerical schemes to compute the solution of the appropriate differential equations. In section 4 we report all parameters necessary to define the model. Next, in section 5 we show computational results for the heart, arterial and venous system, comparing them to literature data and to MRI-derived flow quantification data, where available. In section 6 we discuss results presented and future work. We conclude with section 7, where final considerations are made.

2 Mathematical models

Our closed-loop mathematical model is composed of a one-dimensional network of major arteries, see figure 1, a one-dimensional network of major veins, see figure 2, and lumped parameter models for heart and pulmonary circulation, see figure 3, and for arterioles, capillaries and venules, see figure 4. The numbering in the figures is a guide to the reader to find the geometrical and mechanical properties of vessels in the referred tables.

In the following sections we describe the mathematical models used for each one of these compartments.

2.1 Blood flow in arteries and veins: one-dimensional model

One-dimensional blood flow models result from averaging the incompressible Navier-Stokes equations over the vessel cross-section under some assumptions, including axial symmetry. Also, the structural mechanics of the vessel wall is simplified; relevant assumptions are radial displacement and elastic material properties. For a full derivation of the model see, for example, [35]. Even under such strong simplifications of reality, these models preserve the essential physical features of wave propagation in compliant vessels. The resulting one-dimensional equations for blood flow in elastic vessels are given by the following first-order, non-linear hyperbolic system

$$\begin{cases} \partial_t A + \partial_x q = 0\,, \\ \partial_t q + \partial_x \left(\hat{\alpha} \dfrac{q^2}{A} \right) + \dfrac{A}{\rho} \partial_x p = -f\,, \end{cases} \tag{1}$$

where x is the axial coordinate along the longitudinal axis of the vessel; t is the time; $A(x,t)$ is the cross-sectional area of the vessel; $q(x,t)$ is the flow rate; $p(x,t)$ is the average internal pressure over a cross-section; $f(x,t)$ is the friction force per unit length of the tube; ρ is the fluid density and $\hat{\alpha}$ is a coefficient that depends on the assumed velocity profile. Throughout this work we will take $\hat{\alpha} = 1$, which corresponds to a blunt velocity profile.

To close the system we adopt a tube law, whereby the internal pressure $p(x,t)$ is related to the cross-sectional area $A(x,t)$ and other parameters, namely

$$p(x,t) = p_e(x,t) + \psi(A; A_0, K, P_0)\,. \tag{2}$$

Here $p_e(x,t)$ is the external pressure, prescribed, and $\psi(x,t)$ is the transmural pressure, assumed of the form

$$\psi(A(x,t); K(x), A_0(x), P_0) = K(x)\phi(A(x,t); A_0(x)) + P_0\,. \tag{3}$$

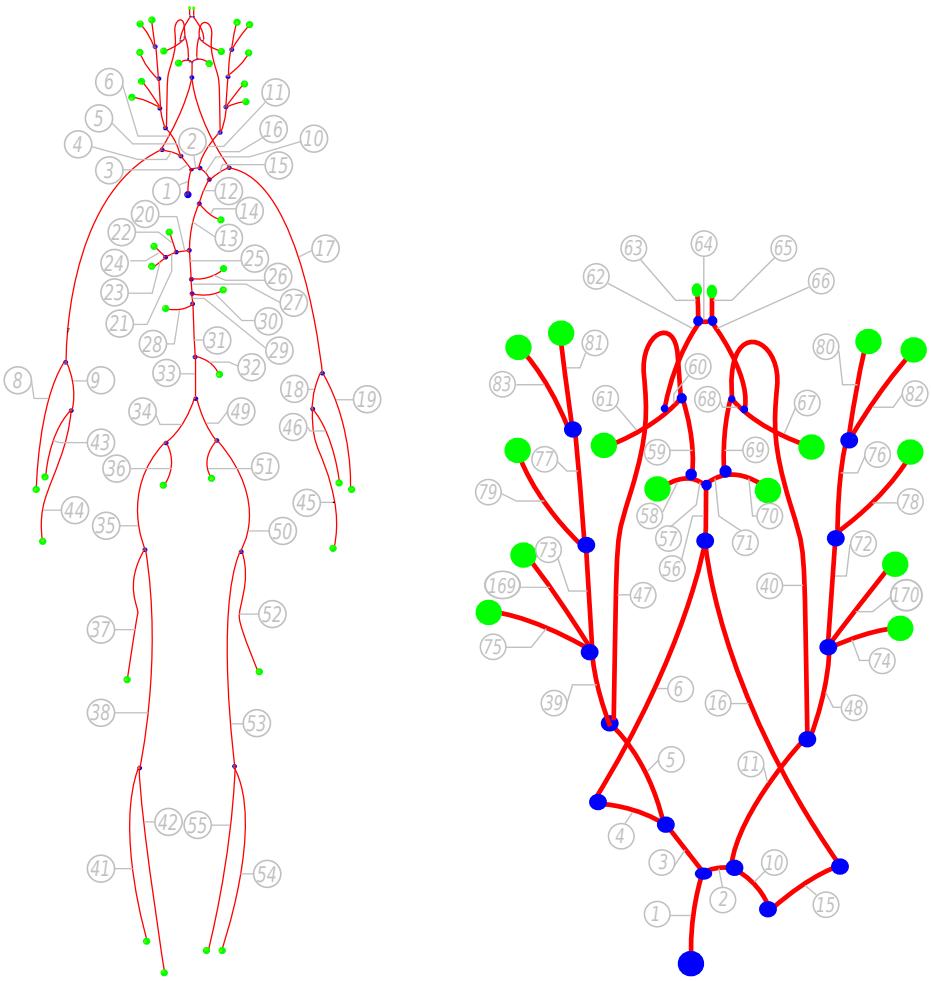

Figure 1: Arterial network composed of 85 arteries, taken from [50] (left). Detail of head and neck arteries (right). Numbers refer to table 3, where geometrical and mechanical parameters for each vessel are reported.

$K(x) = K(E(x), h_0(x))$ is a positive function that contains the combined variation in x of $E(x)$, the Young modulus, and of $h_0(x)$, the wall thickness; see [15] for details. P_0 is the reference pressure for which $A = A_0$, consequently, A_0 is a reference cross-sectional area. The function $\phi(A, x)$ is assumed of the form

$$\phi(A(x,t); A_0(x)) = \left(\frac{A(x,t)}{A_0(x)}\right)^m - \left(\frac{A(x,t)}{A_0(x)}\right)^n . \tag{4}$$

The parameters m and n are obtained from higher-order models or simply computed from experimental measurements. We remark that there are mathematical constraints for the choice of m and n to satisfy hyperbolicity of the equations and for the genuinely non-linear character of the characteristic fields associated with the pressure related eigenvalues; full details are given in [86]. Throughout this work we assume $m > 0$ and $n \in (-2, 0)$. In the next section we discuss the values that K, m and n may assume for different vascular districts.

If one takes into account the spatial variability of A_0, K and p_e and substitutes (2) into (1), the resulting momentum equation reads

$$\partial_t q + \partial_x \left(\hat{\alpha}\frac{q^2}{A}\right) + \frac{A}{\rho} K \phi_A \partial_x A = -\frac{A}{\rho}\left(\partial_x p_e + K\phi_{A_0}\partial_x A_0 + \phi \partial_x K\right) - f\,, \tag{5}$$

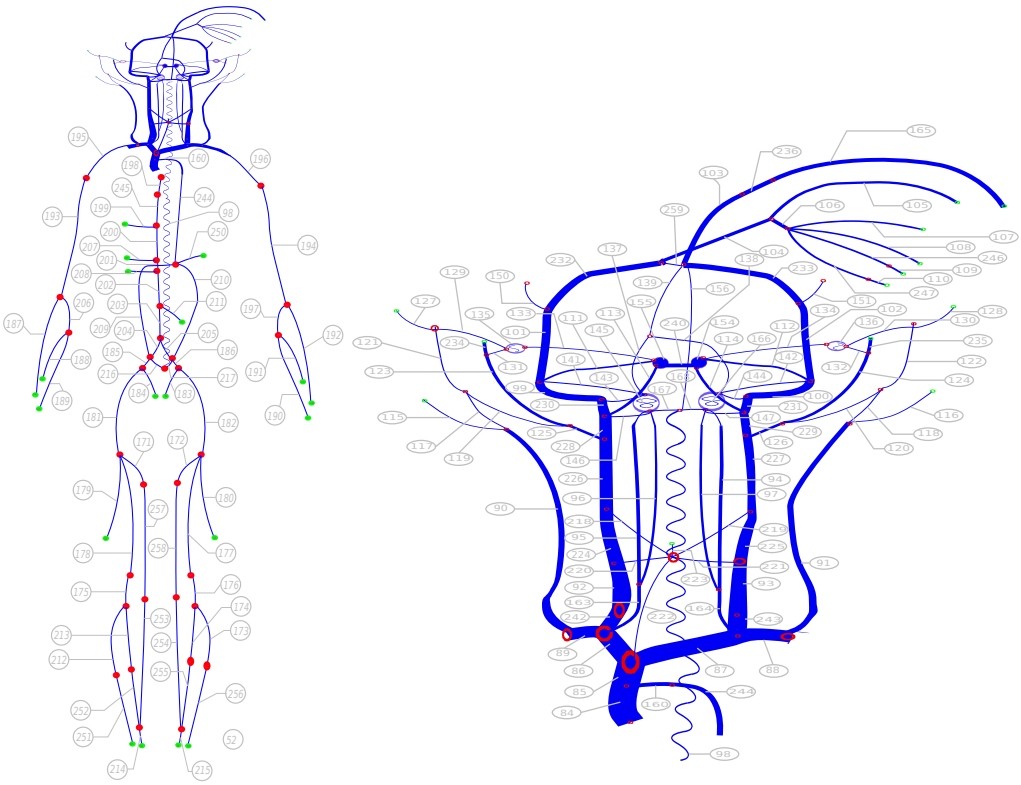

Figure 2: Schematic representation of venous network (left). Detail of head and neck veins (right). Numbers refer to table 8, where geometrical and mechanical parameters for each vessel are reported.

where

$$\phi_A = \frac{\partial \phi}{\partial A}\,, \quad \phi_{A_0} = \frac{\partial \phi}{\partial A_0}\,. \tag{6}$$

The right-hand-side of the momentum balance equation includes *geometric-type* source terms. It is a well-documented fact that a naive discretization of such terms may lead to serious numerical difficulties and hence a careful treatment of these is required [69, 60, 59]. To this end we adopt a reformulation of system (1) proposed in [86], namely

$$\partial_t \mathbf{Q} + \mathbf{A}(\mathbf{Q})\partial_x \mathbf{Q} = \boldsymbol{S}(\boldsymbol{Q})\,, \tag{7}$$

where the state vector $\mathbf{Q}$ is given by

$$\mathbf{Q} = \left[A, q, K, A_0, p_e\right]^T \tag{8}$$

and the coefficient matrix $\mathbf{A}(\mathbf{Q})$ is

$$\mathbf{A}(\mathbf{Q}) = \begin{bmatrix} 0 & 1 & 0 & 0 & 0 \\ c^2 - u^2 & 2u & \frac{A}{\rho}\phi & K\frac{A}{\rho}\phi_{A_0} & \frac{A}{\rho} \\ 0 & 0 & 0 & 0 & 0 \\ 0 & 0 & 0 & 0 & 0 \\ 0 & 0 & 0 & 0 & 0 \end{bmatrix}. \tag{9}$$

Here $u = q/A$ is the cross-sectional averaged velocity of the fluid, $\boldsymbol{S}(\boldsymbol{Q})$ is a source term vector

$$\boldsymbol{S}(\boldsymbol{Q}) = [0, -f, 0, 0, 0]^T \tag{10}$$

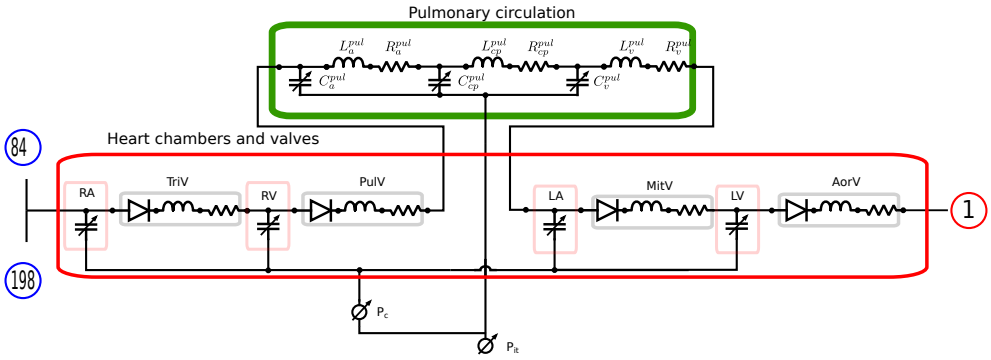

Figure 3: Lumped parameter model for heart and pulmonary circulation. RA, LA: right and left atrium; RV, LV: right and left ventricles. $TriV, PulV, MitV, AorV$: tricuspid, pulmonary, mitral and aortic valves. P_c and P_{it} are pericardium and intra-thoracic pressures, respectively. In the present work both pressures are put equal to zero.

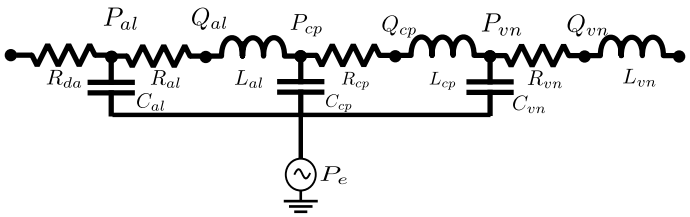

Figure 4: Lumped parameter network for a simple artery-vein connection. Arteries are connected to veins via arterioles, capillaries and venules. For each compartment we specify compliance C, inductance L and resistance R.

and c is the wave speed

$$c = \sqrt{\frac{A}{\rho}\frac{\partial \psi}{\partial A}}\,. \tag{11}$$

Note that all geometric source terms have disappeared from the right hand side and are now in the principal part of the equations.

The eigenvalues of (9) are

$$\lambda_1 = u - c\,, \quad \lambda_2 = \lambda_3 = \lambda_4 = 0\,, \quad \lambda_5 = u + c \tag{12}$$

and the corresponding right eigenvectors of $\boldsymbol{A}(\boldsymbol{Q})$ are

$$\begin{aligned}
\boldsymbol{R}_1 &= \gamma_1 \begin{bmatrix} 1 \\ u-c \\ 0 \\ 0 \\ 0 \end{bmatrix}, \quad \boldsymbol{R}_2 = \gamma_2 \begin{bmatrix} \frac{A}{\rho}\frac{\phi}{u^2-c^2} \\ 0 \\ 1 \\ 0 \\ 0 \end{bmatrix}, \quad \boldsymbol{R}_3 = \gamma_3 \begin{bmatrix} \frac{A}{\rho}\frac{K\phi_{A_0}}{u^2-c^2} \\ 0 \\ 0 \\ 1 \\ 0 \end{bmatrix}, \\
\boldsymbol{R}_4 &= \gamma_4 \begin{bmatrix} \frac{A}{\rho}\frac{1}{u^2-c^2} \\ 0 \\ 0 \\ 0 \\ 1 \end{bmatrix}, \quad \boldsymbol{R}_5 = \gamma_5 \begin{bmatrix} 1 \\ u+c \\ 0 \\ 0 \\ 0 \end{bmatrix},
\end{aligned} \tag{13}$$

where γ_i, for $i = 1, ..., 5$, are arbitrary scaling factors.

Under a suitable assumption for coefficients m and n, system (7) is hyperbolic, though not strictly hyperbolic. Hyperbolicity is lost when $|u| = c$, leading to resonance. As noted in [86] there is a possible loss of uniqueness. These aspects of the mathematical model are currently subject of study.

The first and fifth characteristic fields are genuinely non-linear and are associated with shocks and rarefactions, whereas the remaining fields are linearly degenerate and are associated with stationary contact discontinuities. See [86] for conditions on parameters m and n for this to be true. At this point we introduce the Riemann invariants associated with the genuinely non-linear fields

$$\Gamma_1 = u - \int_{A^*}^{A} \frac{c(\tau)}{\tau} d\tau \,, \quad \Gamma_5 = u + \int_{A^*}^{A} \frac{c(\tau)}{\tau} d\tau \,, \tag{14}$$

and the linearly degenerate fields (LD)

$$\Gamma_1^{LD} = p + \frac{1}{2}\rho u^2 \,, \quad \Gamma_2^{LD} = q \,, \tag{15}$$

where A^* is the cross-sectional area at a reference state. These will be needed in discussing boundary conditions.

2.2 Mechanical properties of vessels and tube laws

Transmural pressure for arteries is commonly defined as

$$\psi_a(x,t) = K_a(x)\,\phi_a(A(x,t);A_0(x)) + P_0 = K_a(x)\left(\left(\frac{A(x,t)}{A_0(x)}\right)^{\frac{1}{2}} - 1\right) + P_0 \,, \tag{16}$$

where $A_0(x)$ is the vessel cross-sectional area for which the transmural pressure $\psi_a = P_0$. K_a is given by

$$K_a(x) = \frac{E(x)\,h_0(x))}{(1-\nu^2)\,R_0(x)} \,, \tag{17}$$

where ν is the Poisson ratio, equal to $1/2$ for incompressible solids and R_0 is the vessel radius at reference configuration. Relation (16), in combination with (17) are derived by considering static equilibrium of the vessel wall and small vessel deformations. See [35] for details.

Relation (16) correctly describes wave propagation patterns in arterial networks as extensively confirmed by existing literature, see [8, 1]. Therefore, we use (16) for describing the behaviour of arteries.

On the other hand, transmural pressure for veins is commonly described by

$$\psi_v(x,t) = K_v(x)\,\phi_v(A(x,t);A_0(x)) + P_0 = K_v(x)\left(\left(\frac{A(x,t)}{A_0(x)}\right)^{m} - \left(\frac{A(x,t)}{A_0(x)}\right)^{n}\right) + P_0 \,. \tag{18}$$

Typical values for collapsible tubes, such as veins, are: $m = 10$, $n = -1.5$, see [74]. The vessel stiffness of veins K_v is

$$K_v(x) = \frac{E(x)}{12\,(1-\nu^2)}\left(\frac{h_0(x)}{R_0(x)}\right)^3 \,. \tag{19}$$

.

Relation (19) derives from considerations made for the collapse of thin-walled elastic tubes. When a thin-walled tube collapses, there is a contact region of the internal vessel walls which divides the ross-section into two tubes running in parallel. Flaherty *et al.* [34] derived an exact solution for this buckling behaviour which relates pressure and area as

$$-\frac{p - p_e}{K_v} = \left(\frac{A(x,t)}{A_0(x)}\right)^{-\frac{3}{2}} \,. \tag{20}$$

The validity of relation (20) for thin-walled latex tubes was confirmed in [74], for $A \le A_0$. In practice, one commonly assigns a high value to m, so that for $A \le A_0$ relation (18) behaves as (20).

In order to better understand the implications of using (18) in our mathematical model let us consider an example. Anliker *et al.* [4] measured the speed of pressure waves in the abdominal vena cava of a dog, obtaining values for wave speed c in the range of 2 to 3 m/s. Nippa *et al.* [64] measured wave speeds in different regions of a human in supine position, obtaining values ranging from 0.6 to 3 m/s. This experimental evidence suggests that wave speed values in the venous system range, roughly, from 1 to 3 m/s, as reported in [18]. Let us take numerical values reported in the literature necessary for computing c for a vein: $E = 1 \times 10^5\, Pa$ (table I of [18]) and $h/R_0 = 0.01$. With these values we obtain that $K_a = 1333.33\, Pa$ and $K_v = 0.0111\, Pa$. Taking these parameters, wave speeds for physiological pressure values lay within the above mentioned ranges for both tube laws. For example, for a pressure $p = 5\, mmHg$ we have $c_a = 0.875\, m\, s^{-1}$ and $c_v = 2.0\, m\, s^{-1}$. However, the behaviour of tube law (18) is drastically different from the one obtained using (16). Figure 5 shows pressure vs non-dimensional area $\alpha = A/A_0$ for the tube laws for arteries and veins, as well as their respective operative pressure ranges. The highly non-linear behaviour of the curve for veins contrasts sharply with that for arteries; veins are tremendously deformable, as compared to arteries; veins collapse while arteries do not. The highly non-linear behaviour of veins implies a judicious choice of numerical methods, on which the robustness of the full model depends.

For a subject in supine position, pressure changes along the venous system are small and deviations from a reference state will be small as well. Therefore, for this posture we expect that the global model will not be excessively sensitive to mechanical properties of veins. On the other hand, changes in posture will induce significant changes in pressure and consequently in the geometry of veins. Above the right atrium, neck veins will collapse and there will be a displacement of around $500 - 600\, ml$ of blood from the upper part of the body to the lower limbs [48]. These changes will crucially depend on the mechanical properties of veins.

It is important to remark that experimental evidence shows that the behaviour of veins in the collapse region is not as extreme as described by relation (18) with stiffness coefficient (19). Bassez *et al.* [10] measured pressure-area relations for lower limb veins, showing a slower collapse process. Even though they did not measured pressure directly, they extrapolated it from height differences between the point where the cross-section of the vein was measured and the right atrium, the validity of the description of the shape of the pressure-area relationship remains. Drzewiecki *et al.* [26] provide the same kind of evidence for a canine jugular vein, though here the non-linear character of the vein collapse is stronger than for lower limb veins. Moreover, Bassez *et al.* [10] performed an *in-vitro* study in which they assessed the influence of a surrounding gel on the collapse dynamics of thin-walled tubes. They showed that collapse tends to be less abrupt as the Young modulus of the surrounding gel increases. This fact confirms *in-vivo* measurements mentioned above, indicating that the fact that veins are attached to external tissue, or at least surrounded by it, will attenuate the collapse dynamics.

Considering the lack of data on mechanical properties of veins we have chosen to use, as a first approach, tube law (18) with coefficients $m = 10$ and $n = -3/2$. Taking into account the considerations made in the previous paragraph, vessel stiffness K_v will not be computed using (19), but will be estimated from pulse wave velocities, following a similar approached as the one used in [62]. We define a function for reference wave speeds in veins as

$$c_0 = c_{0,max} - (c_{0,max} - c_{0,min}) \left(\frac{r - r_{min}}{r_{max} - r_{min}} \right)^{\frac{1}{4}} , \tag{21}$$

where r_{min} and r_{max} are the minimum and maximum vein radii in the network; $c_{0,max} = 3\, m\, s^{-1}$ and $c_{0,min} = 1\, m\, s^{-1}$. Note that reference wave speed c_0 is

$$c_0 = \sqrt{\frac{K_v}{\rho}(m - n)}\, . \tag{22}$$

We set the reference pressure to be used in tube law (18) to $P_0 = 5\, mmHg$. Therefore, we estimate K_v from radii reported in table 8, corresponding to reference pressure P_0, and wave speeds c_0 computed using relation (21). Using this kind of approach, the values for K_v range between 100 and 400 Pa. The

shape of tube law (18) using K_v with values of this order of magnitude can be seen in figure 5. The collapse behaviour of the resulting tube law is still highly non-linear, but not as extreme as the one obtained with K_v computed using relation (19).

The definition of mechanical properties of veins and closure relations remains the major weak point of our model and must be improved in the future. Therefore, we foresee to perform a study as the one presented in [10], especially for neck veins.

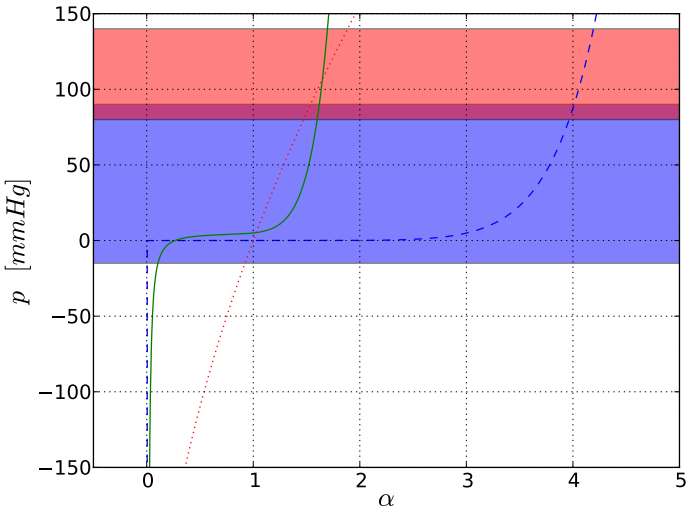

Figure 5: Pressure vs non-dimensional cross-sectional area for tube law (16) with $K_A = 50000\,Pa$ and $P_0 = 0\,mmHg$ (dotted line), for tube law (18) with $K_V = 0.011\,Pa$ and $P_0 = 0\,mmHg$ (dashed line) and for tube law (18) with $K_V = 91.3\,Pa$ and $P_0 = 5\,mmHg$ (continuous line). The top and middle rectangles represent physiological pressure ranges for arteries and veins, respectively.

2.3 Lumped parameter models

Blood flow in arterioles, capillaries and venules is modelled using lumped parameter models, also called 0-D models. These models can be derived from averaging the one dimensional model (1) over the length of a vessel and making several assumptions, such as neglecting the convective term of the momentum equation (see [35] for background). Figure 6 shows a single compartment, composed by a capacitor, a resistor and an inductor. In such a compartment the following equations hold

$$\begin{aligned} \frac{dP}{dt} &= \frac{1}{C}\left(Q_{in} - Q\right) + \frac{dP_e}{dt}\,, \\ \frac{dQ}{dt} &= \frac{1}{L}\left(P - QR - P_{out}\right)\,, \end{aligned} \tag{23}$$

where $Q(t)$ and $P(t)$ are the state variables of the lumped compartment, that is flow rate and pressure, whereas R, L and C are its resistance, inductance and capacitance, respectively. Moreover, P_e represents the external pressure, which will be assumed to be zero if not specified. Q_{in} and P_{out} are variables belonging to other lumped compartments or deriving from boundary conditions, as we shall see later on. Single compartments are then combined to form peripheral beds that connect arteries to veins.

2.4 Heart and pulmonary circulation

For the heart and pulmonary circulation we use a slightly modified version of the lumped parameter model proposed in [83] and extended in [51]. Figure 3 shows the various components of the model,

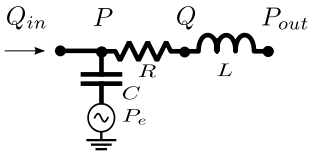

Figure 6: Single compartment used for lumped parameter models. The electric circuit analog comprises a capacitor with capacitance C, a resistor with resistance R and an inductor with inductance L.

including the four heart chambers and corresponding cardiac valves, as well as a simplified compartmental description of the pulmonary circulation, divided in arteries, capillaries and veins.

The model proposed in [51] is based on a prescribed variation in time of heart chambers elastances. Pressure in a cardiac chamber $P_{ch}(t)$ is given by

$$P_{ch}(t) = P_e + (E_A e(t) + E_B)(V_{ch} - V_{ch,0}) + S\frac{dV_{ch}}{dt}\,, \tag{24}$$

where E_A and E_B are the amplitude and baseline values of the elastance, V_{ch} and $V_{ch,0}$ are the current chamber volume and dead chamber volume and S is the viscoelasticity coefficient of the cardiac wall and $e(t)$ is a normalized time-varying function that represents the forcing source for the closed-loop model. The function $e(t)$ differs for ventricles and atria. For atria we use

$$e_a(t) = \begin{cases} \frac{1}{2}\left\{1 + \cos\left[\pi(t + T - t_{ar})/T_{arp}\right]\right\} & 0 \le t \le t_{ar} + T_{arp} - T\,, \\ 0 & t_{ar} + T_{arp} - T < t \le t_{ac}\,, \\ \frac{1}{2}\left\{1 - \cos\left[\pi(t - t_{ac})/T_{acp}\right]\right\} & t_{ac} < t \le t_{ac} + T_{acp}\,, \\ \frac{1}{2}\left\{1 + \cos\left[\pi(t - t_{ar})/T_{arp}\right]\right\} & t_{ac} + T_{acp} < t \le T \end{cases} \tag{25}$$

and for the ventricles

$$e_v(t) = \begin{cases} \frac{1}{2}\left[1 - \cos(\pi t/T_{vcp})\right] & 0 \le t \le T_{vcp}\,, \\ \frac{1}{2}\left\{1 + \cos\left[\pi(t - T_{vcp})/T_{vrp}\right]\right\} & T_{vcp} < t \le T_{vcp} + T_{vrp}\,, \\ 0 & T_{vcp} + T_{vrp} < t \le T_0\,. \end{cases} \tag{26}$$

T_0 is the duration of a cardiac cycle; T_{acp}, T_{vcp}, T_{arp}, and T_{vrp} represent the duration of atrial/ventricular contraction/relaxation, respectively; t_{ac} and t_{ar} are the times within the cardiac cycle at which atrial contraction and relaxation begin.

The flow rate through cardiac valves is modelled using the relation proposed in [51], which describes its time variation as

$$\frac{dQ_{cv}}{dt} = \frac{1}{L_{cv}}\left(\Delta P_{cv} - R_{cv}Q_{cv} - B_{cv}Q_{cv}|Q_{cv}|\right)\,, \tag{27}$$

where L_{cv}, R_{cv} and B_{cv} are coefficients for inertial terms, viscous losses and flow separation, respectively.

Pulmonary circulation is divided into arteries, capillaries and veins. Pressure in each pulmonary compartment is modelled using relation

$$P = E\Phi\,, \tag{28}$$

where Φ is a volume constant and the elastance E is given by

$$E = E_0 e^{V/\Phi}\,, \tag{29}$$

with E_0 being a baseline elastance and V the current volume of the pulmonary compartment. Fluid is exchanged between pulmonary compartments using the second equation in (23). Mass fluxes are then used to update the compartment volume by imposing mass conservation.

In the next section we will describe how each of the mathematical models presented in this section are solved numerically.

3 Numerical methods

As we have seen in section 2, our closed-loop model is composed of a dimensionally heterogeneous spatial domain, comprising one-dimensional and lumped parameter models. The equations for the one-dimensional model are solved using state-of-the-art, high order numerical schemes. Moreover, we have to deal with junctions that may connect several one-dimensional vessels and also with the coupling between one-dimensional and lumped parameter models.

3.1 Numerical scheme for one-dimensional blood flow

System (7) is solved using a high order finite volume-type numerical scheme. High order in space and time is mandatory because of efficiency requirements in order to achieve accurate results at a low cost, as shown in [57] and [59] for the case of one-dimensional blood flow models.

High order accuracy in space and time is achieved by adopting the ADER framework [85]. ADER finite volume schemes consist of two building blocks: a non-linear spatial reconstruction operator and solution of the Generalized Riemann Problem (GRP) at each cell interface to compute numerical fluxes [87]. See also [55] for a discussion on different GRP solvers available. For the solution of the GRP we adopt the Dumbser-Enaux-Toro (DET) solver. This solver was proposed in [28] and extended to non-conservative systems in [27] and [29]. All GRP solvers available, see [55], require a classical Riemann solver (piece-wise constant data). Here we use the Dumbser-Osher-Toro (DOT) Riemann solver [30], as proposed in [59]. The resulting high-order ADER scheme is able to treat venous collapse, as well as transcritical flows [57, 58]. For background on the ADER approach and recent developments see chapters 19 and 20 of [88] and references therein. For alternative approaches see the recent work reported in [20].

As we anticipated in section 2.1, in order to correctly account for the presence of *geometric-type* source terms we have chosen to adopt a reformulation of the classical equations for one-dimensional blood flow models, which implies the use of a well-balanced numerical scheme for this non-conservative system. Therefore, for the computation of a first order monotone numerical flux we use the Dumbser-Osher-Toro (DOT) Riemann solver, put forward in [30] as a modified version of the Osher-Solomon Riemann solver [67] for a conservative hyperbolic system. The DOT scheme has also been extended in [31] to deal with non-conservative hyperbolic systems.

The scheme used in this work was proposed in [59] and is a modification of the original DOT solver, that correctly solves (7). This solver is inspired by the mathematical theory developed by Dal Maso, LeFloch and Murat [23] and may be seen as a path-conservative scheme, as defined in [68].

A finite volume-type path-conservative scheme may be constructed by integrating (7) in space and time in the control volume $[x_{i-\frac{1}{2}}, x_{i+\frac{1}{2}}] \times [t^n, t^{n+1}]$, leading to

$$\boldsymbol{Q}_i^{n+1} = \boldsymbol{Q}_i^n - \frac{\Delta t}{\Delta x}\left(\boldsymbol{D}^-_{i+\frac{1}{2}} + \boldsymbol{D}^+_{i-\frac{1}{2}}\right) + \Delta t \boldsymbol{S}_i - \Delta t \boldsymbol{G}_i^n \,, \tag{30}$$

where

$$\boldsymbol{Q}_i^n = \frac{1}{\Delta x}\int_{x_{i-\frac{1}{2}}}^{x_{i+\frac{1}{2}}} \boldsymbol{Q}(x, t^n)\, dx \,, \tag{31}$$

$$\boldsymbol{G}_i^n = \frac{1}{\Delta t \Delta x}\int_{t^n}^{t^{n+1}} \int_{x_{i-\frac{1}{2}}}^{x_{i+\frac{1}{2}}} \boldsymbol{A}(\boldsymbol{Q})\partial_x \boldsymbol{Q} dx dt \,, \tag{32}$$

$$\boldsymbol{S}_i = \frac{1}{\Delta t \Delta x}\int_{t^n}^{t^{n+1}} \int_{x_{i-\frac{1}{2}}}^{x_{i+\frac{1}{2}}} \boldsymbol{S}(\boldsymbol{Q}(x,t)) dx dt \tag{33}$$

and

$$\boldsymbol{D}^{\pm}_{i+\frac{1}{2}} = \frac{1}{\Delta t}\int_{t^n}^{t^{n+1}} \boldsymbol{\mathcal{D}}^{\pm}_{i+\frac{1}{2}}\left(\boldsymbol{Q}^{-}_{i+\frac{1}{2}}(t), \boldsymbol{Q}^{+}_{i+\frac{1}{2}}(t), \boldsymbol{\Psi}(s)\right) dt\,. \tag{34}$$

Here $\Delta x = x_{i+\frac{1}{2}} - x_{i-\frac{1}{2}}$; $\Delta t = t^{n+1} - t^n$; $\boldsymbol{Q}^{\pm}_{i+\frac{1}{2}}(t)$ are limiting data states from left and right arising in the GRP for system (7) at cell interface $x_{i+\frac{1}{2}}$. Given left and right data $\boldsymbol{Q}^{-}$ and $\boldsymbol{Q}^{+}$ for the Riemann problem at the cell interface $x_{i+\frac{1}{2}}$, $\boldsymbol{\mathcal{D}}^{\pm}\left(\boldsymbol{Q}^{-}, \boldsymbol{Q}^{+}, \boldsymbol{\Psi}(s)\right)$ are defined as fluctuations that depend on a path $\boldsymbol{\Psi}(s)$. We refer the reader to [59] for a detailed description of the numerical scheme. This reference provides a detailed explanation of all the steps necessary to implement the DET solver, as well as to perform the numerical computation of fluctuations via the DOT solver.

3.1.1 Empirical convergence rate

In order to verify that the expected order of accuracy is reached, we perform a numerical convergence rate study. We prescribe a smooth function $\hat{\boldsymbol{Q}}(x,t)$ to be the exact solution. $\hat{\boldsymbol{Q}}(x,t)$ is

$$\hat{\boldsymbol{Q}}(x,t) = \begin{bmatrix} \hat{A}(x,t) \\ \hat{q}(x,t) \\ \hat{K}(x) \\ \hat{A}_0 \\ \hat{p}_e(x) \end{bmatrix} = \begin{bmatrix} \tilde{A} + \tilde{a}\, sin\left(\frac{2\pi}{L}x\right) cos\left(\frac{2\pi}{T_0}t\right) \\ \tilde{q} - \tilde{a}\,\frac{L}{T_0}\, cos\left(\frac{2\pi}{L}x\right) sin\left(\frac{2\pi}{T_0}t\right) \\ \tilde{K} + \tilde{k}\, sin\left(\frac{2\pi}{L}x\right) \\ \tilde{A}_0 + \tilde{a}_0\, sin\left(\frac{2\pi}{L}x\right) \\ \tilde{P}_e + \tilde{p}_e\, sin\left(\frac{2\pi}{L}x\right) \end{bmatrix}. \tag{35}$$

Replacing (35) into (7) we obtain

$$\partial_t \mathbf{Q} + \mathbf{A}(\mathbf{Q})\partial_x \mathbf{Q} = \hat{\mathbf{S}}(x,t)\,. \tag{36}$$

Source term $\hat{\mathbf{S}}(x,t)$ includes terms resulting from the fact that (35) is not a solution of the original system (7). $\hat{\mathbf{S}}(x,t)$ is computed exactly using algebraic manipulators and is not reproduced here for the sake of brevity. For the convergence rate study the following parameters are used: $L = 1.0\,m$, $T_0 = 1.0\,s$, $\tilde{A} = 4.0 \times 10^{-4}\,m^2$, $\tilde{a} = 4.0 \times 10^{-5}\,m^2$, $\tilde{q} = 0.0\,m^3\,s^{-1}$, $\tilde{K} = 50.0\,KPa$, $\tilde{k} = 500.0\,Pa$, $\tilde{P}_e = 0.0\,Pa$, $\tilde{p}_e = 50.0\,Pa$, $m = 1/2$ and $n = 0$. Since we use an explicit numerical scheme, the so called Courant-Friedrichs-Lewy (CFL) condition must be satisfied. In practice, we define our time step by ensuring that the CFL number is smaller than a given threshold. The CFL number is computed as

$$CFL = \lambda^n_{max}\frac{\Delta t}{\Delta x}\,, \tag{37}$$

where λ^n_{max} is the maximum magnitude of eigenvalues (12) in the entire spatial domain at time $t = t^n$. For this test we use a $CFL = 0.9$.

Table 1 displays the empirical convergence rates for the proposed numerical scheme up to fifth-order of accuracy in space and time. Errors were measured in the norms L_1, L_2 and L_∞. The expected convergence rates are reached for all norms. Note that highly accurate computations mean computational efficiency. For a fixed mesh a low order scheme will generally be faster than its higher order extension. On the other hand, if one fixes a given error to be acceptable, high order schemes will satisfy this requirement with considerably less computational effort. Figure 7 shows error versus CPU time for the second and fifth-order implementations of the ADER schemes presented in this paper. The CPU time is that resulting from a sequence of successively refined meshes. It is seen that, for example, given an acceptable error of $E = 10^{-9}$, the fifth-order ADER method will be at least one order of magnitude more efficient than the second-order ADER method.

Scheme	N	L^1	L^2	L^∞	$\mathcal{O}(L^1)$	$\mathcal{O}(L^2)$	$\mathcal{O}(L^\infty)$	$t_{CPU}\,[s]$
ADER-O2	4	1.07e-05	1.23e-05	2.53e-05	-	-	-	0.14
	8	2.47e-06	2.93e-06	7.75e-06	2.1	2.1	1.7	0.42
	16	5.69e-07	6.98e-07	2.02e-06	2.1	2.1	1.9	1.53
	32	1.34e-07	1.69e-07	5.12e-07	2.1	2.0	2.0	3.27
ADER-O3	4	4.24e-06	4.79e-06	8.46e-06	-	-	-	0.39
	8	5.62e-07	6.89e-07	1.46e-06	2.9	2.8	2.5	0.86
	16	7.16e-08	8.95e-08	1.97e-07	3.0	2.9	2.9	1.90
	32	8.99e-09	1.13e-08	2.51e-08	3.0	3.0	3.0	4.13
ADER-O4	4	6.66e-06	1.64e-06	1.65e-05	-	-	-	0.68
	8	4.028e-07	4.88e-07	1.21e-06	4.0	4.0	3.8	1.36
	16	1.92e-08	2.29e-08	6.43e-08	4.4	4.4	4.2	2.24
	32	9.73e-10	1.19e-09	3.69e-09	4.3	4.3	4.1	5.89
ADER-O5	4	1.80e-06	2.02e-06	3.39e-06	-	-	-	7.20
	8	6.88e-08	8.39e-08	1.71e-07	4.7	4.6	4.3	1.38
	16	2.27e-09	2.81e-09	6.01e-09	4.9	4.9	4.8	3.64
	32	8.13e-11	9.72e-11	2.11e-10	4.8	4.9	4.8	9.08

Table 1: Convergence results for the ADER scheme. N is the number of cells. Errors are computed for variable A. CPU times are reported for all tests.

3.1.2 Test with exact solution including an elastic jump

We solve a Riemann problem that intends to resemble the effect of an (idealized) Valsava manoeuvre on an internal jugular vein with incompetent valve and discontinuous mechanical properties. Note that while this test does not correspond to a physiological situation, it is still valid for testing the robustness of the numerical scheme for parameter ranges that are those of human veins.

The vessel length is $L = 0.2\,m$. Initial conditions are discontinuous at $x = 0.06\,m$. States to the left of the discontinuity are $A_L = 0.5\,A_0^L$, $U_L = 0.0\,m\,s^{-1}$, $K^L = K_{ref}$, $A_0^L = 1.0\,A_{ref}$, $p_e^L = 0.0\,mmHg$, while to the right of the discontinuity we set $A_R = 1.\,A_0^R$, $U_R = 0.0\,m\,s^{-1}$, $K^R = 10\,K_{ref}$, $A_0^R = 1.0\,A_{ref}$, $p_e^R = 20.0\,mmHg$. Reference values for vessel stiffness and cross-sectional area are $K_{ref} = 300.0\,Pa$ and $A_{ref} = 1.0 \times 10^{-4}\,m^2$. Initial conditions correspond to a vessel with discontinuous mechanical properties. Moreover, the portion of the vessel to the right of the discontinuity is compressed. Transmural pressure is sub-atmospheric to the left of the discontinuity and $20\,mmHg$ in the rest of the vessel. The exact solution of this problem was computed using an implementation of the exact Riemann solver presented in [86].

The problem was solved numerically using first and third order versions of the numerical schemes considered in this work, using 100 computational cells and a $CFL = 0.9$. Results are shown in figure 8. For $t > 0\,s$ an elastic jump starts travelling to the left of the initial discontinuity, while a rarefaction wave is directed in the opposite direction. Finally, a stationary contact discontinuity is observed in correspondence of discontinuous variations of mechanical properties. Both, the first and high order numerical solutions correctly capture the propagation velocity of non-linear waves (elastic jump and rarefaction) and the states to both sides of the stationary contact discontinuity. The better description of the elastic jump by the third order scheme, as compared to the one given by the first order scheme, is clearly observable.

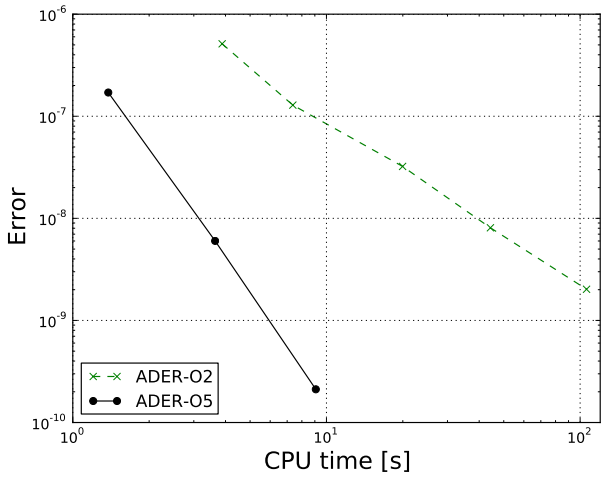

Figure 7: Error versus CPU time for second and fifth-order implementations of the ADER scheme.

3.2 Junctions

The coupling of several one-dimensional vessels at branching points (for arteries) and merging points (for veins) is treated using the methodology proposed in [76], which we formulate here for the case of N_P vessels converging at node P. The computational cell involved in the coupling of the $k-th$ vessel, with $k = 1, ..., N_P$, will provide the state $Q_k^n = [A_k^n, q_k^n]^T$ at time t^n.

In order to couple the N_P vessels, we have to compute the unknowns cross-sectional area A_k^* and velocity u_k^* for each vessel converging at node P, which means that we have $2N_P$ unknowns. Quantities A_k^*, u_k^* will be used to compute fluxes at the terminal interface of the k-th vessel.

Let vessel k be discretised by N_k cells so that its local numbering is $i = 1, ..., N_k$. We define the auxiliary function

$$g_k(I_k) = \begin{cases} 1\,, & \text{if } I_k = N_k\,, \\ -1\,, & \text{if } I_k = 1\,, \end{cases} \tag{38}$$

where I_k is the index of the computational cell of vessel k that converges to node P.

The first N_P equations are given by imposing conservation of mass

$$\sum_{k=1}^{N_P} g_k A_k^* u_k^* = 0 \tag{39}$$

and total pressure

$$p(A_1^*) + \frac{1}{2}\rho(u_1^*)^2 - p(A_k^*) - \frac{1}{2}\rho(u_k^*)^2 = 0, \quad k = 2, ..., N_P\,. \tag{40}$$

The remaining N_P relations are obtained by enforcing that characteristics leave the one-dimensional domain undisturbed

$$u_k^n + g_k \int_{A_{0,k}}^{A_k^n} \frac{c(\tau)}{\tau} d\tau - u_k^* - g_k \int_{A_{0,k}}^{A_k^*} \frac{c(\tau)}{\tau} d\tau = 0 \quad k = 1, ..., N_P\,. \tag{41}$$

Equations (39) to (41) constitute a non-linear system with $2\,N_P$ unknowns and is solved using Newton method.

The main requirements for this procedure to work are that the flow regime is sub-critical and that no elastic jumps reach node P. In fact, numerical investigations not reported in this work have shown

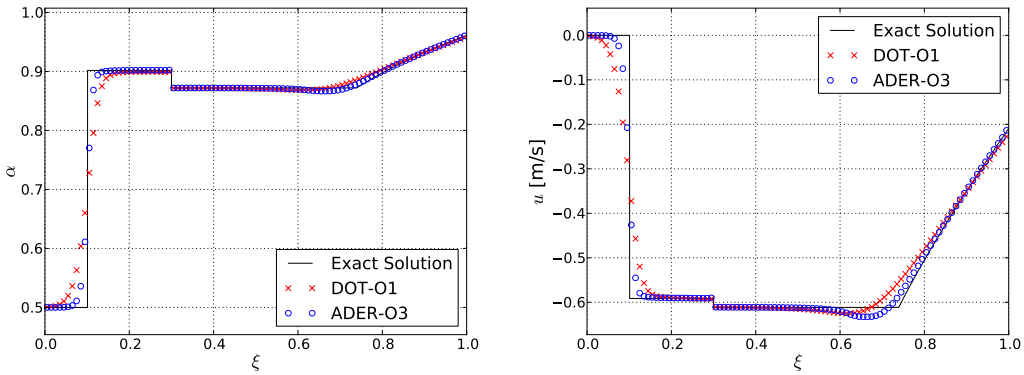

Figure 8: Exact solution and numerical results for the Riemann problem described in section 3.1.2 regarding the effect of an (idealized) Valsava maneuver on an internal jugular vein with incompetent valve and discontinuous mechanical properties. Results for first and third order versions of the numerical schemes used in this work. Results shown for non-dimensional cross-sectional area ($\alpha = A/A_{ref}$) (left) and velocity (right) versus non-dimensional length ($\xi = x/L$).

that this algorithm fails to converge in the case of fast postural changes. Besides the lack of blood flow regulatory mechanisms, this algorithm remains the mayor limitation of the present model in order to be able to perform simulations including postural changes.

3.3 Arterioles, capillaries and venules and 1D-0D matching

For most terminal vessels, arteries are linked to veins via lumped parameter models that include arterioles, capillaries and venules, as shown in figure 4. We call this type of artery-vein connection a *simple connection*, since, as we will see later, some peripheral beds are formed by slightly more complex networks. The resistance of distal arteries, R_{da} is set to be equal to the characteristic impedance of the terminal artery in order to avoid non-physiological wave reflections, as suggested in [2]. The variables to be computed for each circuit are

- boundary conditions for the 1D-0D interface (artery-distal arteries): P^*_{art} and Q^*_{art},
- state variables for each lumped compartment: P_{al}, Q_{al}, P_{cp}, Q_{cp} , P_{vn} and Q_{vn}.

In order to correctly couple terminal arteries to arterioles we follow the methodology proposed in [2]. First, we impose that forward travelling waves leave the arterial domain undisturbed

$$\Gamma_5(P_{art}, Q_{art}) - \Gamma_5(P^*_{art}, Q^*_{art}) = 0\,, \tag{42}$$

where Γ_5 are Riemann invariants associated to forward travelling characteristics and P_{art}, Q_{art} are pressure and flow rate values for the last computational cell of the one-dimensional domain of the terminal artery. Moreover, we note that, for the pressure drop across R_{da}, the following relation must hold

$$Q^*_{art} = \frac{P^*_{art} - P_{al}}{R_{da}}\,. \tag{43}$$

For state variables in lumped compartments we discretise equations (23) using a backward Euler scheme. For the 0D-1D interface (venules-veins), we impose $P_{out} = P_{vein}$ and $Q_{vein} = Q_{vn}$.

Equations (42), (43), together with a backward Euler discretization of equations (23) for arterioles, capillaries and venules, yield a differential-algebraic system with 8 unknowns which is solved at each time step using a Newton method.

3.4 Boundary conditions

Boundary conditions other than branching and merging points are treated using the same approach applied to junctions. That is, we impose that the characteristic that leaves the one-dimensional domain is not disturbed by boundary conditions, while we impose a given flow rate q^*_{bc} or a pressure $p(A^*_{bc})$. In the case of fixed flow rate q^*_{bc} we compute A^*_{bc} by imposing that

$$\frac{q^n_{1D}}{A^n_{1D}} + g_{1D}\int_{A_{0,1D}}^{A^n_{1D}} \frac{c(\tau)}{\tau} d\tau - \frac{q^*_{bc}}{A^*_{bc}} - g_{1D}\int_{A_{0,1D}}^{A^*_{bc}} \frac{c(\tau)}{\tau} d\tau = 0\,, \tag{44}$$

where q^n_{1D} and A^n_{1D} are flow rate and pressure at the terminal computational cell of the vessel and g_{1D} is given by (38). On the other hand, if we need to prescribe a pressure $p(A^*_{bc})$, we solve (44) for q^*_{bc}. This type of boundary conditions is applied to the proximal end of the ascending aorta, to distal ends of terminal veins and to the proximal end of the cavas at their interface with the right atrium.

In the next section we will present all parameters necessary for the description of the arterial and venous networks, as well as for the various lumped parameter models used in this work.

4 Physiological data

One-dimensional vessels are characterized by a network topology, vessel geometry and mechanical properties. Moreover, lumped parameter models presented in section 2 make use of several parameters. In this section we present all parameters necessary for the implementation of our closed-loop model.

4.1 Geometry and parameters

Arteries. The arterial network, shown in figure 1, is composed by 85 arteries and was entirely taken from [50] and references therein. Table 3 reports geometrical parameters and wave speed c_0 assigned to each artery. Reported radii correspond to a baseline internal pressure $P_0 = 85.\, mmHg$ and therefore to $A = A_0$, as proposed in [51]. Mechanical parameters are obtained from c_0, by solving (11) for K, with tube law (16) and $A = A_0$. Table 2 reports the reference of location codes appearing in the next-to-last column of table 3.

Code	Location
1	Dural sinuses
2	Extra-cranial
3	Neck
4	Thorax
5	Abdomen
6	Upper limbs
7	Lower limbs
8	Pelvis
9	Intra-cranial

Table 2: Location codes indicated in tables 3 and 8.

Heart and pulmonary circulation. Parameters for heart and pulmonary circulation were taken from [51] and [83] and are reported in tables 4 and 5, respectively.

Terminal segments. Most arteries are connected to veins via a simple artery-vein connection. However, for several compartments there is a distribution of flow from one systemic artery to multiple veins or single arteries feeding more veins. These compartments are denoted as *lumped models* A to G. Figures

9 to 11 show the corresponding circuits, whereas tables 6 and 7 report the value of parameters for each compartment.

Veins.

The venous network is shown in figure 2. Geometrical and mechanical parameters are reported in table 8. The last column of this table reports the source from which geometrical information for each venous segment was extracted. Reported radii correspond to a baseline internal pressure $P_0 = 5.\, mmHg$ and therefore to $A = A_0$. c_0 is the wave speed (21), from which K_v can be estimated. Note that relation (21) is used for all veins expect for dural sinuses, for which a $c_0 = c_{0,max}$ was used.

Since a major motivation of this work regards the study of neurovascular diseases recently linked to the venous vasculature of the head and neck, as explained in section 1, this area is described with more emphasis compared to other regions of the venous network. Most of the major veins of this region were obtained via a segmentation procedure on a patient-specific basis. Medical imaging data used in this paper has been provided by the Magnetic Resonance Research Facility at the Wayne State University, Detroit, USA. In particular, we used 2D Time-of-Flight (TOF) and 3D contrast-enhanced MR-Venography (CE-MRV) sequences of the head and neck of healthy controls. Figure 12 (top) shows a Maximum Intensity Projection (MPI) of a TOF image for a healthy control. The geometry of major vessels was extracted using the open-source segmentation tool Vascular Modelling Toolkit (VMTK) [5]. Once the 3D domain is available, VMTK allows to compute centerlines and vessel cross-sectional area (CSA) for user-defined vessels. Figure 12 (bottom) shows segmentation results, as well as the centerline for a left internal jugular vein (IJV). The geometry of major head and neck veins presented in this work is from a single healthy control. The characterization of the model with patient-specific head and neck veins can be easily carried out within a few hours.

Venous valves are described by the same model used for cardiac valves, with parameters: $R = 0.003\, mmHg\, s\, ml^{-1}$, $L = 0.0025\, mmHg\, s^2\, ml^{-1}$ and $B = 0.000025\, mmHg\, s^2\, ml^{-2}$. These parameters are similar to the ones used for cardiac valves but allow for a faster opening/closure of the venous valve. Table 9 shows the location of valves in the venous network.

No.	Vessel name	$L\ [cm]$	$r_0\ [cm]$	$r_1\ [cm]$	$c_0\ [m/s]$	Loc.	Ref.
1	Ascending aorta	2.00	1.525	1.420	5.110	4	[51]
2	Aortic arch I	3.00	1.420	1.342	5.110	4	[51]
3	Brachiocephalic a.	3.50	0.650	0.620	5.910	4	[51]
4	R. subclavian a. I	3.50	0.425	0.407	5.290	6	[51]
5	R. carotid a.	17.70	0.400	0.370	5.920	3	[51]
6	R. vertebral a.	13.50	0.150	0.136	11.900	3	[51]
7	R. subclavian a. II	39.80	0.407	0.230	5.380	6	[51]
8	R. radius	22.00	0.175	0.140	10.120	6	[51]
9	R. ulnar a. I	6.70	0.215	0.215	8.780	6	[51]
10	Aortic arch II	4.00	1.342	1.246	5.110	4	[51]
11	L. carotid a.	20.80	0.400	0.370	5.920	3	[51]
12	Thoracic aorta I	5.50	1.246	1.124	5.110	4	[51]
13	Thoracic aorta II	10.50	1.124	0.924	5.110	4	[51]
14	Intercostal a.	7.30	0.300	0.300	7.130	4	[51]
15	L. subclavian a. I	3.50	0.425	0.407	5.290	6	[51]
16	L. vertebral a.	13.50	0.150	0.136	11.900	3	[51]
17	L. subclavian a. II	39.80	0.407	0.230	5.380	6	[51]
18	L. ulnar a. I	6.70	0.215	0.215	8.780	6	[51]
19	L. radius	22.00	0.175	0.140	10.120	6	[51]
20	Celiac a. I	2.00	0.350	0.300	5.860	5	[51]
21	Celiac a. II	2.00	0.300	0.250	6.540	5	[51]
22	Hepatic a.	6.50	0.275	0.250	6.860	5	[51]
23	Splenic a.	5.80	0.175	0.150	7.220	5	[51]
24	Gastric a.	5.50	0.200	0.200	6.400	5	[51]
25	Abdominal aorta I	5.30	0.924	0.838	5.110	5	[51]
26	Sup. mesenteric a.	5.00	0.400	0.350	5.770	5	[51]
27	Abdominal aorta II	1.50	0.838	0.814	5.110	5	[51]
28	R. renal a.	3.00	0.275	0.275	6.050	5	[51]
29	Abdominal aorta III	1.50	0.814	0.792	5.110	5	[51]
30	L. renal a.	3.00	0.275	0.275	6.050	5	[51]
31	Abdominal aorta IV	12.50	0.792	0.627	5.110	5	[51]
32	Inf. mesenteric a.	3.80	0.200	0.175	6.250	5	[51]
33	Abdominal aorta V	8.00	0.627	0.550	5.110	5	[51]
34	R. com. iliac a.	5.80	0.400	0.370	5.500	8	[51]
35	R. ext. iliac a.	14.50	0.370	0.314	7.050	8	[51]
36	R. int. iliac a.	4.50	0.200	0.200	10.100	8	[51]
37	R. deep femoral a.	11.30	0.200	0.200	7.880	7	[51]
38	R. femoral a.	44.30	0.314	0.275	8.100	7	[51]
39	R. ext. carotid a. I	4.10	0.200	0.150	8.900	2	[51]
40	L. int. carotid a. I	17.60	0.250	0.200	7.900	3	[51]
41	R. post. tibial a.	34.40	0.175	0.175	11.980	7	[51]
42	R. ant. tibial a.	32.20	0.250	0.250	9.780	7	[51]
43	R. interosseous a.	7.00	0.100	0.100	15.570	6	[51]
44	R. ulnar a. II	17.00	0.203	0.180	12.530	6	[51]
45	L. ulnar a. II	17.00	0.203	0.180	12.530	6	[51]
46	L. interosseous a.	7.00	0.100	0.100	15.570	6	[51]
47	R. int. carotid a. I	17.60	0.250	0.200	7.900	3	[51]
48	L. ext. carotid a. I	4.10	0.200	0.150	8.900	3	[51]
49	L. com. iliac a.	5.80	0.400	0.370	5.500	8	[51]
50	L. ext. iliac a.	14.50	0.370	0.314	7.050	8	[51]
51	L. int. iliac a.	4.50	0.200	0.200	10.100	8	[51]
52	L. deep femoral a.	11.30	0.200	0.200	7.880	7	[51]
53	L. femoral a.	44.30	0.314	0.275	8.100	7	[51]
54	L. post. tibial a.	34.40	0.175	0.175	11.980	7	[51]
55	L. ant. tibial a.	32.20	0.250	0.250	9.780	7	[51]
56	Basilar a.	2.90	0.162	0.162	9.330	1	[50]
57	R. post. cerebral. a. I	0.50	0.107	0.107	12.930	1	[50]
58	R. post. cerebral. a. II	8.60	0.105	0.105	13.130	1	[50]
59	R. post. communicating a.	1.50	0.073	0.073	17.240	1	[50]
60	R. int. carotid a. II	0.50	0.200	0.200	8.260	1	[50]
61	R. mid. cerebral a.	11.90	0.143	0.143	10.230	1	[50]
62	R. ant. cerebral a. I	1.20	0.117	0.117	12.030	1	[50]
63	R. ant. cererbal a. II	10.30	0.120	0.120	11.770	1	[50]
64	Ant. communicating a.	0.30	0.100	0.100	17.080	1	[50]
65	L. ant. cerebral a. II	10.30	0.120	0.120	11.770	1	[50]
66	L. ant. cerebral a. I	1.20	0.117	0.117	12.030	1	[50]
67	L. mid. cerebral a.	11.90	0.143	0.143	10.230	1	[50]
68	L. int. carotid a. II	0.50	0.200	0.200	8.260	1	[50]
69	L. post. communicating a.	1.50	0.073	0.073	17.240	1	[50]
70	L. post. cerebral a. II	8.60	0.105	0.105	13.130	1	[50]
71	L. post. cerebral a. I	0.50	0.107	0.107	12.930	1	[50]
72	L. ext. carotid a. II	6.10	0.200	0.200	8.530	3	[50]
73	R. ext. carotid a. II	6.10	0.200	0.200	8.530	3	[50]
74	L. sup. thyroid a.	10.10	0.100	0.100	16.570	3	[50]
75	R. sup. thyroid a.	10.10	0.100	0.100	16.570	3	[50]
76	L. superf. temporal a.	6.10	0.160	0.160	9.620	2	[50]
77	R. superf. temporal a.	6.10	0.160	0.160	9.620	2	[50]
78	L. maxillary a.	9.10	0.110	0.110	15.090	2	[50]
79	R. maxillary a.	9.10	0.110	0.110	15.090	2	[50]
80	L. superf. temp. fron. bran.	10.00	0.110	0.110	15.090	2	[50]
81	R. superf. temp. fron. bran.	10.00	0.110	0.110	15.090	2	[50]
82	L. superf. temp. pari. bran.	10.10	0.110	0.110	15.090	2	[50]
83	R. superf. temp. pari. bran	10.10	0.110	0.110	15.090	2	[50]
169	R. facial a.	11.60	0.130	0.130	15.090	2	[50]
170	L. facial a.	11.60	0.130	0.130	15.090	2	[50]

Table 3: Physiological data for arteries, taken from [50] and references therein. L: length; r_0: inlet radius; r_1: outlet radius; c_0: wave speed for $A = A_0$; *Loc*: location in the body according to table 2; *Ref*: bibliographic source.

	RA	RV	LA	LV	TriV	PulV	MitV	AorV
E_A $[mmHg\,ml^{-1}]$	0.06	0.55	0.07	2.75	–	–	–	–
E_B $[mmHg\,ml^{-1}]$	0.05	0.05	0.09	0.08	–	–	–	–
T_{cp} $[s]$	0.17	0.30	0.17	0.30	–	–	–	–
T_{rp} $[s]$	0.17	0.15	0.17	0.15	–	–	–	–
t_c $[s]$	0.80	0.00	0.80	0.00	–	–	–	–
T_r $[s]$	0.97	0.30	0.97	0.30	–	–	–	–
S $[mmHg\,s\,ml^{-1}]$	$P_{ra}\times$ 0.00050	$P_{ra}\times$ 0.00050	$P_{ra}\times$ 0.00050	$P_{ra}\times$ 0.00050	–	–	–	–
B $[mmHg\,s^2\,ml^{-2}]$	–	–	–	–	0.000016	0.000025	0.000016	0.000025
R $[mmHg\,s\,ml^{-1}]$	–	–	–	–	0.001	0.003	0.001	0.003
L $[mmHg\,s^2\,ml^{-1}]$	–	–	–	–	0.0002	0.0005	0.0002	0.0005

Table 4: Parameters for heart chambers and cardiac valves, modified from [50] and references therein. RA: right atrium; RV: right ventricle; LA: left atrium; LV: left ventricle; $TriV$: tricuspid valve; $PulV$: pulmonary valve; $MitV$: mitral valve; $AorV$: aortic valve.

	E_0 $[mmHg\,ml^{-1}]$	Φ $[ml]$	R $[mmHg\,s\,ml^{-1}]$	L $[mmHg\,s^2\,ml^{-1}]$	S $[mmHg\,s\,ml^{-1}]$
Artery	0.02	20.0	0.040	0.0005	0.01
Capillary	0.02	60.0	0.040	0.0005	0.01
Vein	0.02	200.0	0.005	0.0005	0.01

Table 5: Parameters for pulmonary circulation, modified from [50] and [83]. E_0: baseline elastance; Φ: volume constant; R: resistance; L: inductance; S: viscoelasticity.

A. index	V. index	R_{da}	R_{al}	L_{al}	C_{al}	R_{cp}	L_{cp}	C_{cp}	R_{vn}	L_{vn}	C_{vn}
8	187	13.5055	17.0300	0.0180	0.0140	6.5500	0.0029	0.0014	2.1000	0.0052	0.0430
43	188	39.4048	393.7000	0.0700	0.0043	151.4000	0.0117	0.0004	48.5000	0.0209	0.0129
44	189	9.9182	19.6900	0.0180	0.0140	7.5700	0.0029	0.0014	2.4200	0.0052	0.0430
45	190	9.9182	19.6900	0.0180	0.0140	7.5700	0.0029	0.0014	2.4200	0.0052	0.0430
46	191	39.4048	393.7000	0.0700	0.0043	151.4000	0.0117	0.0004	48.5000	0.0209	0.0129
19	192	13.5055	17.0300	0.0180	0.0140	6.5500	0.0029	0.0014	2.1000	0.0052	0.0430
41	251	9.9001	30.4400	0.0210	0.0500	11.7100	0.0035	0.0010	3.7500	0.0062	0.0310
42	214	3.9602	14.0300	0.0140	0.1150	5.4000	0.0023	0.0023	1.7300	0.0042	0.0680
37	179	4.9857	13.3700	0.0140	0.1150	5.1400	0.0023	0.0023	1.6500	0.0042	0.0680
55	215	3.9602	14.0300	0.0140	0.1150	5.4000	0.0023	0.0023	1.7300	0.0042	0.0680
54	256	9.9001	30.4400	0.0210	0.0500	11.7100	0.0035	0.0010	3.7500	0.0062	0.0310
52	180	4.9857	13.3700	0.0140	0.1150	5.1400	0.0023	0.0023	1.6500	0.0042	0.0680
36	184	6.3903	23.4800	0.0180	0.0182	9.0300	0.0030	0.0014	2.8900	0.0054	0.1080
51	183	6.3903	23.4800	0.0180	0.0182	9.0300	0.0030	0.0014	2.8900	0.0054	0.1080
32	211	4.8972	30.7400	0.0200	0.0178	11.8500	0.0033	0.0011	3.7800	0.0060	0.0330
28	208	2.0247	4.3100	0.0080	0.0680	1.6600	0.0014	0.0067	0.5300	0.0024	0.2000
30	207	2.0247	4.3100	0.0080	0.0680	1.6600	0.0014	0.0067	0.5300	0.0024	0.2000
169	234	22.5976	119.6200	0.0170	0.0150	46.0070	0.0029	0.0015	14.7220	0.0051	0.0450
170	235	22.5976	119.6200	0.0170	0.0150	46.0070	0.0029	0.0015	14.7220	0.0051	0.0450
14	250	2.0050	5.6100	0.0090	0.1390	2.1600	0.0015	0.0139	0.6900	0.0027	0.4170

Table 6: Parameters for simple artery-vein connections, modified from [50] and references therein. The first two columns show the indexes of the linked artery and the linked vein, according to tables 3 and 8. The third column shows the resistance of distal arteries R_{da} $[mmHg\,ml^{-1}]$, while the remaining columns report resistance R $[mmHg\,ml^{-1}]$, inductance L $[mmHg\,s^2\,ml^{-1}]$ and capacitance C $[ml\,mmHg^{-1}]$ for arterioles, capillaries and venules respectively.

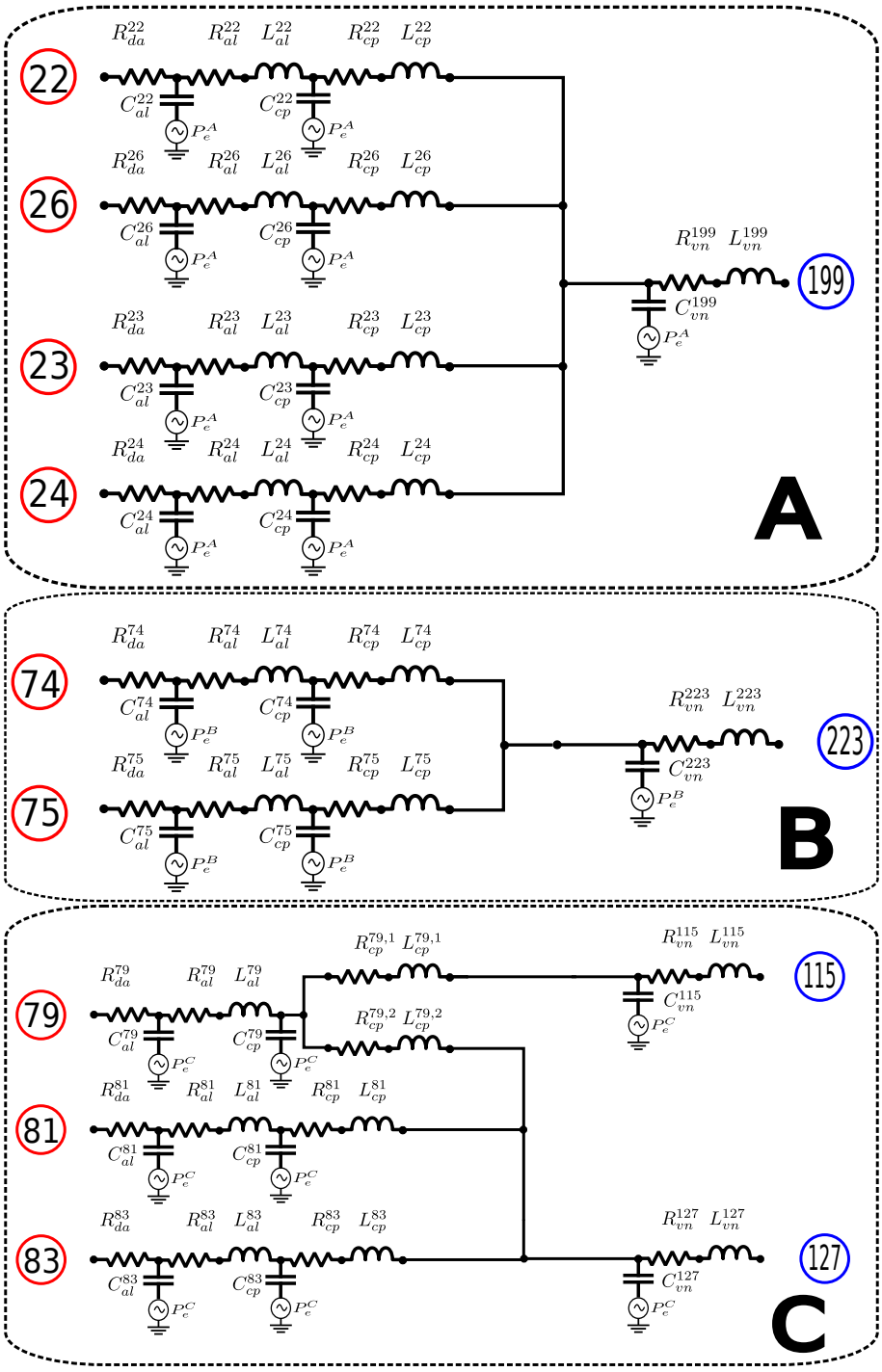

Figure 9: Lumped models A to C. The figure shows the indexes of feeding arteries, to the left, and collecting veins, to the right. Parameters for resistances, inductors and capacitors are found in table 7.

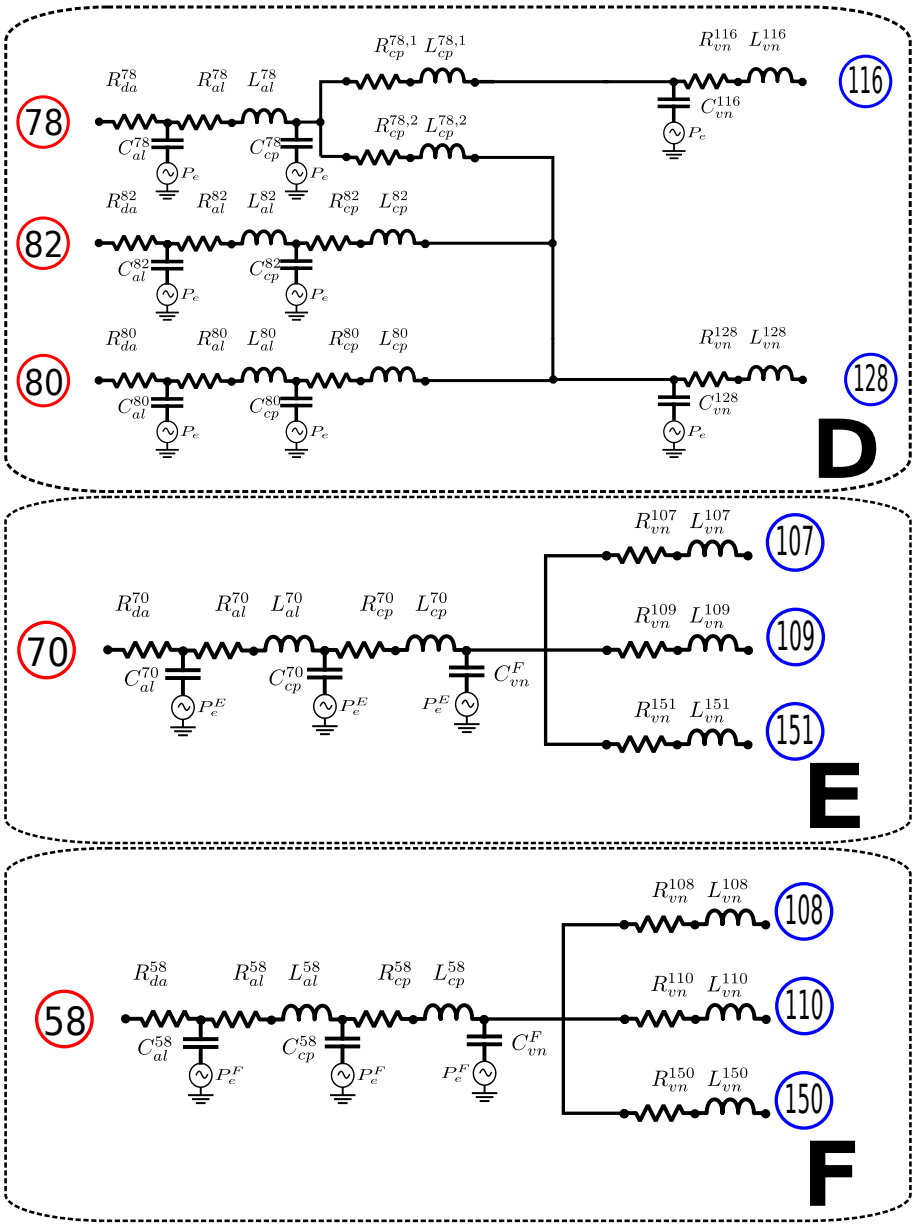

Figure 10: Lumped models D to F. The figure shows the indexes of feeding arteries, to the left, and collecting veins, to the right. Parameters for resistances, inductors and capacitors are found in table 7.

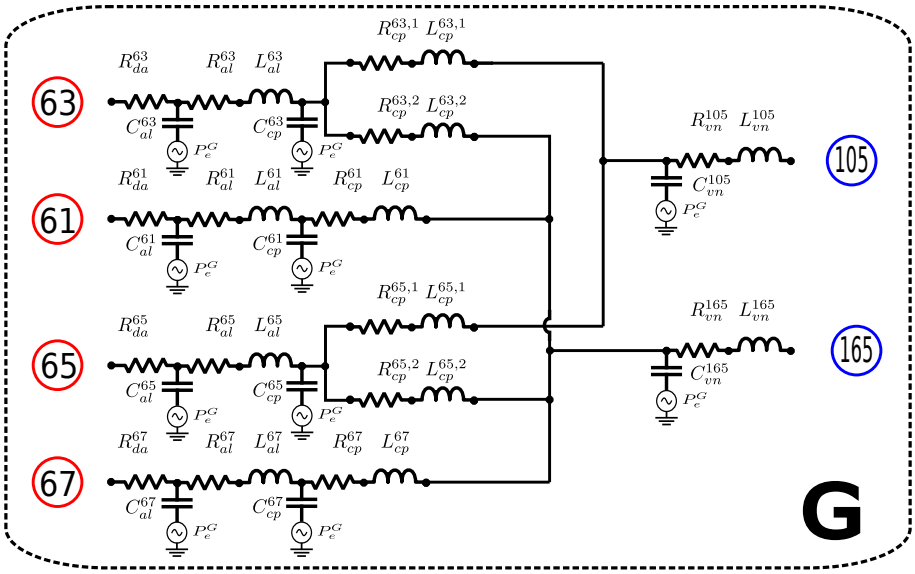

Figure 11: Lumped model G. The figure shows the indexes of feeding arteries, to the left, and collecting veins, to the right. Parameters for resistances, inductors and capacitors are found in table 7.

Parent/daughter vessel	R_{da}	R_{al}	L_{al}	C_{al}	R_{cp}	L_{cp}	C_{cp}	R_{vn}	L_{vn}	C_{vn}
Lumped model A										
22	2.7594	16.2400	0.0150	0.0210	6.2400	0.0024	0.0021	–	–	–
26	1.1634	3.8500	0.0070	0.0810	1.4800	0.0012	0.0081	–	–	–
23	7.8931	21.3300	0.0180	0.0140	8.2000	0.0030	0.0014	–	–	–
24	4.0493	8.9100	0.0120	0.0330	3.4300	0.0019	0.0032	–	–	–
199	–	–	–	–	–	–	–	0.2550	0.0013	0.5270
Lumped model B										
74	41.9356	119.6200	0.0878	0.0037	46.0070	0.0140	0.0004	–	–	–
75	41.9356	119.6200	0.0878	0.0037	46.0070	0.0140	0.0004	–	–	–
223	–	–	–	–	–	–	–	7.3610	0.0129	0.0225
Lumped model C										
79	31.5620	101.8600	0.0748	0.0037	78.3560	0.0244	0.0004	–	–	–
	–	–	–	–	78.3560	0.0244	–	–	–	–
81	31.5620	101.8600	0.0748	0.0037	39.1780	0.0122	0.0004	–	–	–
83	31.5620	102.5100	0.0753	0.0037	39.4200	0.0123	0.0004	–	–	–
115	–	–	–	–	–	–	–	25.0740	0.0440	0.0056
127	–	–	–	–	–	–	–	5.0260	0.0088	0.0281
Lumped model D										
78	31.5620	101.8600	0.0748	0.0037	78.3560	0.0244	0.0004	–	–	–
	–	–	–	–	78.3560	0.0244	–	–	–	–
82	31.5620	101.8600	0.0748	0.0037	39.1780	0.0122	0.0004	–	–	–
80	31.5620	102.5100	0.0753	0.0037	39.4200	0.0123	0.0004	–	–	–
116	–	–	–	–	–	–	–	25.0740	0.0440	0.0056
128	–	–	–	–	–	–	–	5.0260	0.0088	0.0281
Lumped model E										
70	30.1402	18.7300	0.0138	0.0070	7.2000	0.0022	0.0007	–	–	–
common param.	–	–	–	–	–	–	–	–	–	0.0018
107	–	–	–	–	–	–	–	18.4400	0.0324	–
109	–	–	–	–	–	–	–	18.4400	0.0324	–
151	–	–	–	–	–	–	–	3.0700	0.0054	–
Lumped model F										
58	30.1402	18.7300	0.0138	0.0070	7.2000	0.0022	0.0007	–	–	–
common param.	–	–	–	–	–	–	–	–	–	0.0018
108	–	–	–	–	–	–	–	18.4400	0.0324	–
110	–	–	–	–	–	–	–	18.4400	0.0324	–
150	–	–	–	–	–	–	–	3.0700	0.0054	–
Lumped model G										
63	20.6859	24.4500	0.0179	0.0070	18.8100	0.0059	0.0007	–	–	–
	–	–	–	–	18.8100	0.0059	–	–	–	–
65	20.6859	24.4500	0.0179	0.0070	18.8100	0.0059	0.0007	–	–	–
61	12.6609	10.5700	0.0078	0.0140	18.8100	0.0059	0.0014	–	–	–
	–	–	–	–	4.0700	0.0013	–	–	–	–
67	12.6609	10.5700	0.0078	0.0140	4.0700	0.0013	0.0014	–	–	–
105	–	–	–	–	–	–	–	3.7800	0.0066	0.0210
165	–	–	–	–	–	–	–	0.6900	0.0016	0.0210

Table 7: Parameters for complex artery-vein connections, shown in figures 9 to 11, derived from [51]. Parameter units are the same as the ones used in table 6.

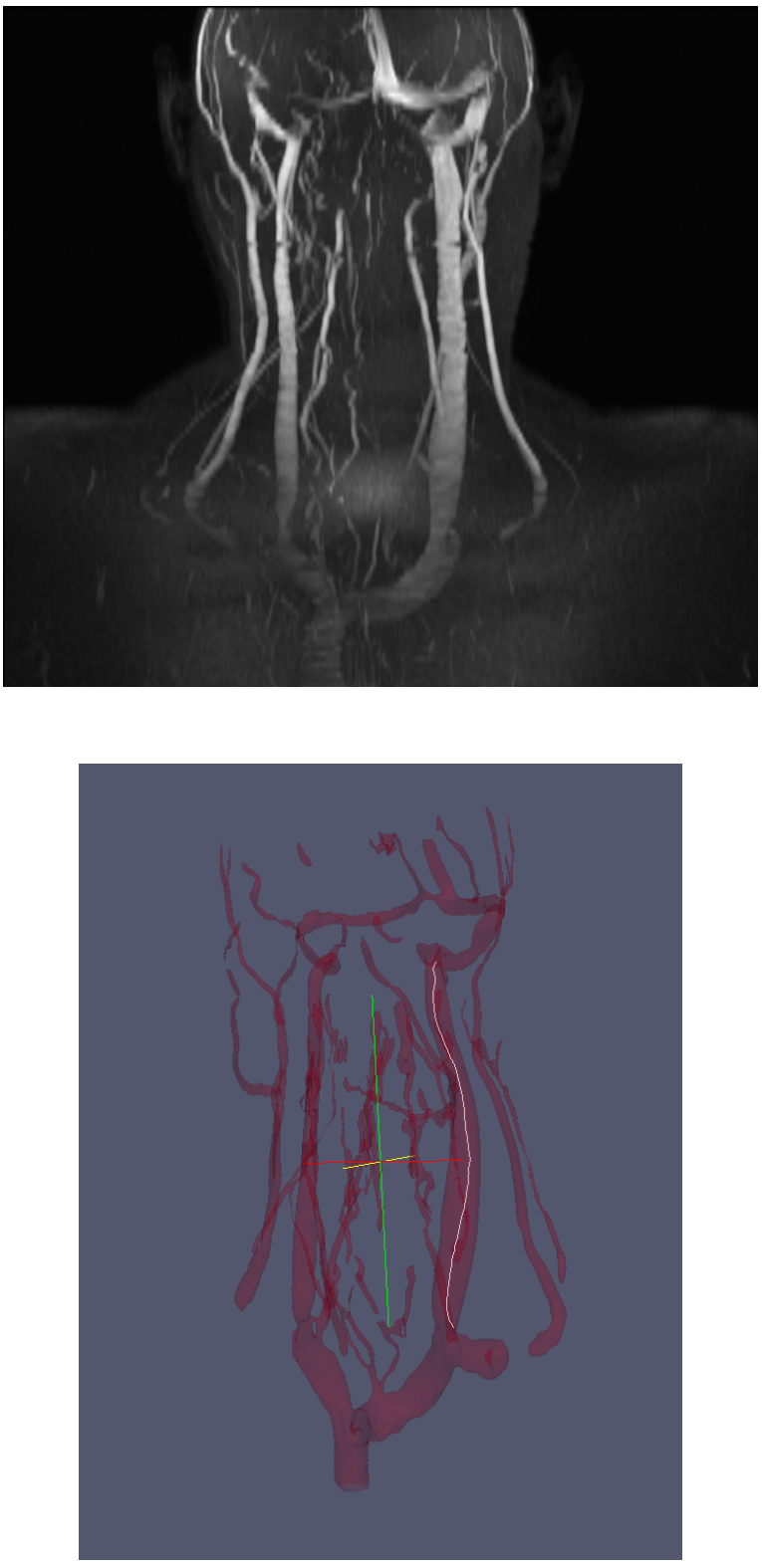

Figure 12: MIP-TOF for a healthy patient (top) and patient-specific segmented geometry and centerline extraction for head and neck veins (bottom).

Table 8: Geometrical and mechanical parameters for the venous system. L: length; r_0: inlet radius; r_1: outlet radius; c_0: wave speed for $A = A_0$; Loc location in the body according to table 2; Ref : bibliographic source or MRI imaging segmented geometry.

No.	Vessel name	$L\ [cm]$	$r_0\ [cm]$	$r_1\ [cm]$	$c_0\ [m/s]$	Loc.	Ref.
84	Sup. vena cava I	1.50	0.800	0.800	1.000	4	MRI
85	Sup. vena cava II	2.00	0.800	0.800	1.000	4	MRI
86	R. brachiocephalic v.	4.00	0.564	0.564	1.360	4	MRI
87	L. brachiocephalic v.	7.50	0.535	0.535	1.410	4	MRI
88	L. subclavian v. I	3.00	0.564	0.564	1.360	6	[36], [75]
89	R. subclavian v. I	3.00	0.564	0.564	1.360	6	[36], [75]
90	R. ext. jugular v.	20.00	0.252	0.252	2.022	3	MRI
91	L. ext. jugular v.	20.00	0.252	0.357	1.883	3	MRI
92	R. int. jugular v. I	2.50	0.399	0.399	1.669	3	MRI
93	L. int. jugular v. I	2.50	0.564	0.618	1.315	3	MRI
94	L. vertebral v. II	11.00	0.138	0.160	2.381	3	MRI
95	R. vertebral v. II	11.00	0.138	0.160	2.381	3	MRI
96	R. deep cervical v.	13.00	0.160	0.160	2.333	3	MRI
97	L. deep cervical v.	13.00	0.160	0.160	2.333	3	MRI
98	Vertebral venous plexus	71.00	0.368	0.368	1.735	3	[82]
99	R. sigmoid sinus II	3.50	0.252	0.252	3.000	1	MRI
100	L. sigmoid sinus II	3.50	0.357	0.378	3.000	1	MRI
101	R. trans. sinus I	3.50	0.218	0.178	3.000	1	MRI
102	L. trans. sinus I	3.50	0.437	0.309	3.000	1	MRI
103	Sup. sagittal sinus I	10.00	0.319	0.367	3.000	1	MRI
104	Straight sinus	4.00	0.250	0.250	3.000	1	MRI
105	Inf. sagittal sinus	11.00	0.160	0.160	3.000	1	MRI
106	Vein of Galen	1.60	0.309	0.400	1.765	9	MRI
107	L. int. cerebral v.	5.00	0.126	0.126	2.494	9	MRI
108	R. int. cerebral v.	5.00	0.126	0.126	2.494	9	MRI
109	L. basal v. of Rosenthal I	1.00	0.126	0.126	2.494	9	MRI
110	R. basal v. of Rosenthal I	1.00	0.126	0.126	2.494	9	MRI
111	R. sup. petrosal sinus	5.70	0.149	0.149	3.000	1	MRI
112	L. sup. petrosal sinus	5.70	0.149	0.149	3.000	1	MRI
113	R. inf. petrosal sinus	3.20	0.080	0.160	3.000	1	MRI
114	L. inf. petrosal sinus	3.20	0.080	0.160	3.000	1	MRI
115	R. post. auricular v.	5.00	0.080	0.080	3.000	2	MRI
116	L. post. auricular v.	5.00	0.080	0.080	3.000	2	MRI
117	R. post. retromandibular v.	3.52	0.250	0.250	2.028	2	[92]
118	L. post. retromandibular v.	3.52	0.250	0.250	2.028	2	[92]
119	R. ant. retromandibular v.	3.15	0.235	0.235	2.072	2	[92]
120	L. ant. retromandibular v.	3.15	0.235	0.235	2.072	2	[92]
121	R. retromandibular v.	4.50	0.260	0.260	2.000	2	[92]
122	L. retromandibular v.	4.50	0.260	0.260	2.000	2	[92]
123	R. facial v. II	6.00	0.132	0.178	2.355	2	MRI
124	L. facial v. II	6.00	0.132	0.178	2.355	2	MRI
125	R. com. facial v.	0.90	0.180	0.180	2.255	2	MRI
126	L. com. facial v.	0.90	0.180	0.180	2.255	2	MRI
127	R. superf. temp. v.	5.00	0.190	0.190	2.218	2	[92]
128	L. superf. temp. v.	5.00	0.190	0.190	2.218	2	[92]
129	R. maxillary v.	1.00	0.175	0.175	2.274	2	[92], MRI
130	L. maxillary v.	1.00	0.175	0.175	2.274	2	[92], MRI
131	R. deep facial v.	0.90	0.250	0.250	2.028	2	–
132	L. deep facial v.	0.90	0.250	0.250	2.028	2	–
133	R. emissary v.	3.00	0.100	0.100	2.667	2	[84]
134	L. emissary v.	3.00	0.100	0.100	2.667	2	[84]
135	R. pterygoid plexus	0.90	0.150	0.150	2.376	2	[79]
136	L. pterygoid plexus	0.90	0.150	0.150	2.376	2	[79]
137	R. marginal sinus	4.00	0.100	0.100	3.000	1	[19]
138	L. marginal sinus	4.00	0.100	0.100	3.000	1	[19]
139	Occipittal sinus	3.50	0.235	0.235	3.000	1	[9]
141	R. mastoid emissary v.	7.20	0.175	0.175	2.274	2	[93, 53]
142	L. mastoid emissary v.	7.20	0.175	0.175	2.274	2	[93, 53]
143	R. post. condylar v.	3.00	0.315	0.315	1.857	2	MRI, [19]
144	L. post. condylar v.	3.00	0.315	0.315	1.857	2	MRI, [19]
145	R. subocc. sinus	1.00	0.450	0.450	1.566	2	[19]
146	R. lat. ant. condylar v.	3.00	0.315	0.315	1.857	2	[19]
147	L. lat. ant. condylar v.	3.00	0.315	0.315	1.857	2	[19]
150	R. Labbe v.	5.00	0.126	0.126	2.494	9	MRI
151	L. Labbe v.	5.00	0.126	0.126	2.494	9	MRI
154	L. cavernous sinus	1.50	0.100	0.100	3.000	1	MRI
155	R. cavernous sinus	1.50	0.100	0.100	3.000	1	MRI
156	Occipittal v.	5.00	0.126	0.126	2.494	2	MRI
160	Azygos v. I	2.00	0.425	0.425	1.616	4	MRI, [47]
163	R. vertebral v. I	5.00	0.160	0.160	2.333	3	MRI
164	L. vertebral v. I	5.00	0.160	0.160	2.333	3	MRI
165	Sup. sagittal sinus III	13.00	0.200	0.319	3.000	1	MRI
166	L. subocc. sinus	1.00	0.450	0.450	1.566	2	[19]
167	R. anastomotic v.	2.00	0.100	0.100	2.667	3	[19], [6]
168	L. anastomotic v.	2.00	0.100	0.100	2.667	3	[19], [6]
171	R. great saphenous v. I	7.50	0.222	0.230	2.100	7	[95], [3]
172	L. great saphenous v. I	7.50	0.222	0.230	2.100	7	[95], [3]
173	L. post. tibial v. I	17.30	0.150	0.150	2.376	7	[46], [3]
174	L. ant. tibial v. I	16.00	0.150	0.150	2.376	7	[46], [3]
175	R. popliteal v.	19.00	0.340	0.340	1.798	7	[41], [3]
176	L. popliteal v.	19.00	0.340	0.340	1.798	7	[41], [3]
177	L. femoral v.	25.40	0.350	0.350	1.775	7	[41], [3]
178	R. femoral v.	25.40	0.350	0.350	1.775	7	[41], [3]
179	R. deep femoral v.	12.60	0.350	0.350	1.775	7	[3]
180	L. deep femoral v.	12.60	0.350	0.350	1.775	7	[3]
181	R. ext. iliac v.	14.40	0.500	0.500	1.472	8	[41], [3]
182	L. ext. iliac v.	14.40	0.500	0.500	1.472	8	[41], [3]
183	L. int. iliac v.	5.00	0.150	0.150	2.376	8	[41], [3]
184	R. int. iliac v.	5.00	0.150	0.150	2.376	8	[41], [3]
185	R. com. iliac v. II	2.00	0.575	0.575	1.342	8	[66], [3]
186	L. com. iliac v. II	2.00	0.575	0.575	1.342	8	[66], [3]
187	R. radial v.	40.60	0.200	0.200	2.184	6	[3]

Table 8 – continued from previous page

No.	Vessel name	$L\ [cm]$	$r_0\ [cm]$	$r_1\ [cm]$	$c_0\ [m/s]$	Loc.	Ref.
188	L. interosseous v.	7.00	0.100	0.100	2.667	6	[3]
189	R. ulnar v. II	30.60	0.200	0.200	2.184	6	[3]
190	L. ulnar v. II	30.60	0.200	0.200	2.184	6	[3]
191	L. interosseous v.	7.00	0.100	0.100	2.667	6	[3]
192	L. radial v.	40.60	0.200	0.200	2.184	6	[3]
193	L. subclavian v. III	27.00	0.520	0.520	1.437	6	[36], [75]
194	R. subclavian v. III	27.00	0.520	0.520	1.437	6	[36], [75]
195	L. subclavian v. II	3.00	0.520	0.520	1.437	6	[36], [75]
196	R. subclavian v. II	3.00	0.520	0.520	1.437	6	[36], [75]
197	L. ulnar v. I	10.00	0.200	0.200	2.184	6	[3]
198	Inf. vena cava I	2.00	0.762	0.762	1.053	5	[24], [3]
199	Hepatic v.	6.80	0.485	0.485	1.500	5	[25], [3]
200	Inf. vena cava II	1.50	0.762	0.762	1.053	5	[24], [3]
201	inf. vena cava III	1.50	0.762	0.762	1.053	5	[24], [3]
202	Inf. vena cava IV	12.50	0.762	0.762	1.053	5	[24], [3]
203	Inf. vena cava V	8.00	0.762	0.762	1.053	5	[24], [3]
204	R. com. iliac v. I	3.80	0.575	0.575	1.342	8	[66], [3]
205	L. com. iliac v. I	3.80	0.575	0.575	1.342	8	[66], [3]
206	R. ulnar v. I	10.00	0.200	0.200	2.184	6	[3]
207	L. renal v.	3.20	0.250	0.250	2.028	5	[3]
208	R. renal v.	3.20	0.250	0.250	2.028	5	[3]
209	Ascending lumbar v.	23.00	0.200	0.200	2.184	5	[79]
210	hemiazygos v.	23.00	0.280	0.280	1.946	5	[79]
211	Inf. mesenteric v.	6.00	0.450	0.450	1.566	5	[3]
212	R. post. tibial v. I	17.30	0.150	0.150	2.376	7	[46], [3]
213	R. ant. tibial v. I	16.00	0.150	0.150	2.376	7	[46], [3]
214	R. ant. tibial v. II	2.00	0.600	0.600	1.300	7	[46], [3]
215	L. ant. tibial v. II	2.00	0.600	0.600	1.300	7	[46], [3]
216	R. lumbar v.	3.80	0.100	0.100	2.667	5	[79]
217	L. lumbar v.	3.80	0.100	0.100	2.667	5	[79]
218	R. sup. thyroid v.	4.00	0.150	0.150	2.376	3	MRI, [91]
219	L. sup. thyroid v.	4.00	0.150	0.150	2.376	3	MRI, [91]
220	R. mid. thyroid v.	3.00	0.100	0.100	2.667	3	MRI, [91]
221	L. mid. thyroid v.	3.00	0.100	0.100	2.667	3	MRI, [91]
222	Inf. thyroid v.	7.00	0.126	0.126	2.494	3	MRI
223	Thyroid connection	2.00	0.160	0.160	2.333	3	–
224	R. int. jugular v. II	3.00	0.357	0.357	1.759	3	MRI
225	L. int. jugular v. II	3.00	0.564	0.564	1.360	3	MRI
226	R. int. jugular v. III	2.70	0.252	0.357	1.883	3	MRI
227	L. int. jugular v. III	2.70	0.564	0.564	1.360	3	MRI
228	R. int. jugular v. IV	6.80	0.252	0.252	2.022	3	MRI
229	L. int. jugular v. IV	6.80	0.399	0.564	1.506	3	MRI
230	R. sigmoid sinus I	1.50	0.252	0.252	3.000	1	MRI
231	L. sigmoid sinus I	1.50	0.378	0.399	3.000	1	MRI
232	R. trans. sinus II	3.50	0.178	0.252	3.000	1	MRI
233	L. trans. sinus II	3.50	0.309	0.357	3.000	1	MRI
234	R. facial v. I	2.00	0.113	0.132	2.514	2	MRI
235	L. facial v. I	2.00	0.113	0.132	2.514	2	MRI
236	Sup. sagittal sinus II	2.00	0.319	0.319	3.000	1	MRI
240	Intra-cavernous sinus	2.00	0.126	0.126	3.000	1	[79], [19]
242	R. int. jugular v. V	1.00	0.399	0.399	1.669	3	MRI
243	L. int. jugular v. V	1.00	0.618	0.618	1.271	3	MRI
244	Azygos v. II	28.00	0.425	0.425	1.616	4	MRI, [47]
245	Inf. vena cava VI	13.30	0.762	0.762	1.053	5	[66], [3]
246	L. basal v. of Rosenthal II	7.00	0.126	0.126	2.494	9	MRI
247	R. basal v. of Rosenthal II	7.00	0.126	0.126	2.494	9	MRI
250	Intercostal v.	2.00	0.400	0.400	1.667	4	[79]
251	R. post. tibial v. II	17.30	0.150	0.150	2.376	7	[46], [3]
252	R. ant. tibial v. II	16.00	0.150	0.150	2.376	7	[46], [3]
253	R. great saphenous v. II	37.50	0.145	0.188	2.308	7	[95], [3]
254	L. great saphenous v. II	37.50	0.145	0.188	2.308	7	[95], [3]
255	L. ant. tibial v. II	16.00	0.150	0.150	2.376	7	[46], [3]
256	L. post. tibial v. I	17.30	0.150	0.150	2.376	7	[46], [3]
257	R. great saphenous v. III	30.00	0.188	0.222	2.168	7	[95], [3]
258	L. great saphenous v. III	30.00	0.188	0.222	2.168	7	[95], [3]
259	Confluence of sinuses	1.00	0.010	0.010	3.000	1	MRI

4.2 Flow measurements

In addition to morphological data, Phase-Contrast (PC) MRI flow quantification data was gathered by the MR Research Facility at the Wayne State University, Detroit (USA) and made available for the validation of our model. Flow was acquired in the neck at three levels and for dural sinuses, including the Superior Sagittal Sinus, the Straight Sinus and both Transverse Sinuses. Figure 13 shows the three acquisition planes for neck veins and the acquisition plane for dural sinuses. Flow measurements were performed in the same MRI session when TOF and CE-MRV sequences were acquired, so that morphological and flow quantification data are patient-specific. PC-MRI sequences were processed with an in-house tool of the MR Research Facility in order to extract time resolved flow rates over the cardiac cycle [33]. A maximum encoding velocity (VENC) of $50\,cm\,s^{-1}$ was used. For a detailed description of the acquisition procedure refer to [33].

After having presented physiological data necessary for the construction of our closed-loop model, we proceed in the next section with a thorough validation of our computational results, comparing them versus literature data and to PC-MRI flow quantification data.

No.	Left vessel index	Right vessel index
1	193	195
2	194	196
3	244	160
4	257	171
5	258	172
6	253	257
7	254	258
8	175	178
9	176	177
10	251	212
11	256	173
12	252	213
13	255	174
14	92	242
15	93	243

Table 9: Location of valves in the venous network shown in figure 2. Valves allow flow from left to right vessel.

5 Computational results

In this section we present computational results in order to perform a thorough validation of our closed-loop model. The one-dimensional domain was divided into cells with a length of $\Delta x = 1\,cm$, imposing however a minimum of 3 computational cells in each vessel. Setting the CFL number of $CFL = 0.9$, the average time step was equal to $1.5 \times 10^{-4}\,s$. We note that the time step is computed at each computational step. Other relevant parameters are blood viscosity $\mu = 0.0045\,Pa\,s$ and density $\rho = 1050\,kg\,m^{-3}$. Initial velocity was set to $u = 0\,m\,s^{-1}$ everywhere and initial pressures were chosen as reported in table 10. We note that the specification of initial conditions is crucial, especially in the case of a closed-loop model, since they will define the periodic condition that the model will reach. The model reached a periodic state after approximately 15 cardiac cycles. For friction loses we assume a Poiseuille velocity profile so that $f = 8\pi\mu\,u/\rho$. All computations were performed using a third order accurate version of our numerical scheme.

Compartment	$P_{ini}\,[mmHg]$
Arteries	70.0
Veins	5
Heart chambers & pulmonary compartments	10.0
Arterioles	45.0
Capillaries	25.0
Venules	10.0

Table 10: Inital pressure values for all compartments.

5.1 Heart

Figure 14 shows computed pressures and volumes for each cardiac chamber. Pressure variation over the cardiac cycle well represents physiological conditions, for both atria and ventricles. The same observation is valid for volume curves. Stroke volume of the left ventricle is around $80\,ml$, in accordance with physiological values [48].

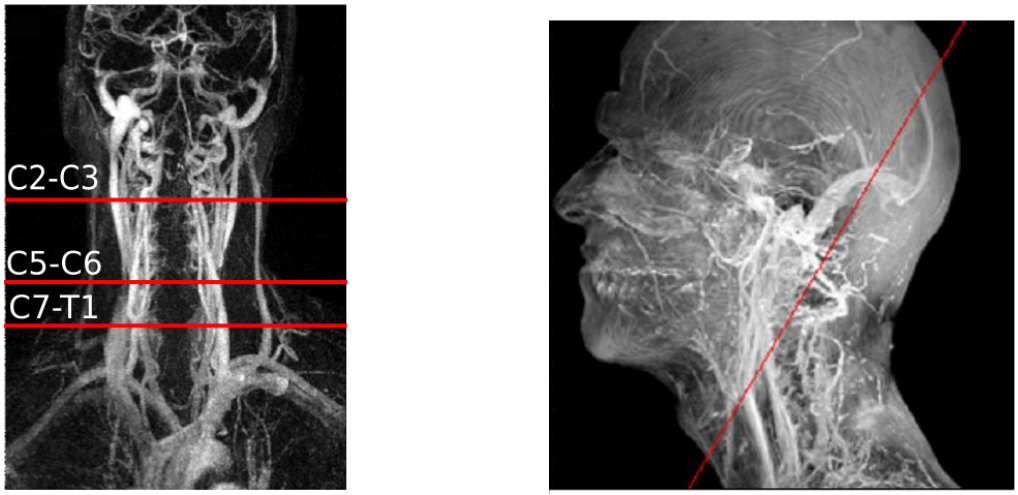

Figure 13: Planes at which PC-MRI flow measures were acquired for neck veins at C2-C3, C5-C6 and C7-T1 levels (left) and for dural sinuses (right). The three acquisition planes along the neck allow to evaluate how flow rate increases as tributary veins merge the internal jugular veins, whereas the acquisition plane for dural sinues allows the evaluation of flow for the Superior Sagittal Sinus, the Straight Sinus and both Transverse Sinuses.

5.2 Arteries

Figures 15 and 16 show a comparison between computational results and data reported in the literature for average flow rates in major systemic arteries and cerebral arteries, respectively. The agreement is satisfactory in both cases, with computational results always located within physiological ranges.

Figures 17 and 18 show computed pressure and flow rate along the aorta and major leg arteries. Pressure waveforms in systemic arteries well reproduce physiological patterns, with steepening of the wave and increase in systolic peak pressure as the wave travels away from the heart. Pressure ranges in the arterial system fall within normal values. Pulse pressure in the ascending aorta is equal to $40\,mmHg$, while it reaches a value of $66\,mmHg$ in the femoral artery.

Computed pressure and flow rate in head and neck arteries are shown in figure 19. While correct flow distribution was already assessed in figure 16, flow waveforms correspond to measurements reported in [38] and [72].

5.3 Capillary beds

Figure 20 shows computed pressure in arterioles, capillaries and venules at selected locations in lumped compartments E to G. Pressure values in all compartments vary around physiologically reasonable values: $40 - 60\,mmHg$ for arterioles, $20 - 30\,mmHg$ for capillaries and $13 - 17\,mmHg$ for venules.

5.4 Veins

Figure 21 shows a comparison of computed mean flow rates in selected systemic veins vs data reported in the literature. The agreement is satisfactory, showing a correct distribution of venous return between superior vena cava (SVC) and inferior vena cava (IVC).

Regarding average flow rates in head and neck veins, in figure 22 we compare our computational results with patient-specific PC-MRI flow quantification data. Flow distribution between Superior Sagittal Sinus (SSS) and Straight Sinus (StS) and consequently between both Transverse Sinuses (TS) matches measured data. Flow distribution between left and right Internal Jugular Veins (IJVs) correctly represents measurements, with an increase of flow as we move from C2-C3 level to C5-C6 level. The increased

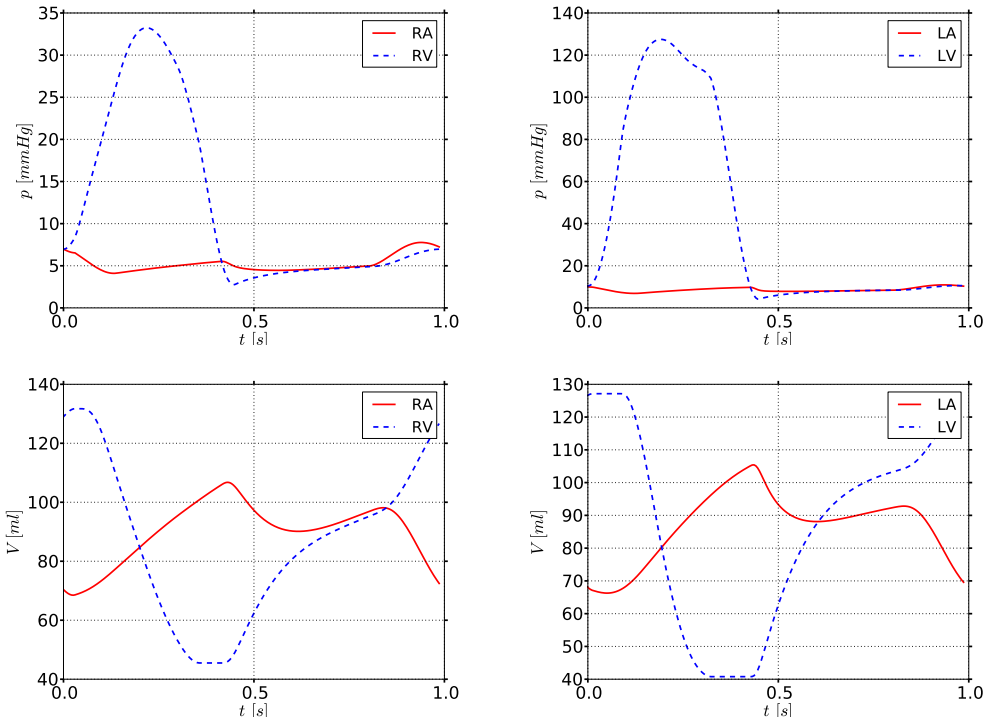

Figure 14: Computed pressures (top) and volumes (bottom) for the four cardiac chambers. RA: Right Atrium; RV: Right Ventricle; LA: Left Atrium; LV: Left Ventricle.

flow rate is related to the contribution of collaterals, such as the common facial vein and thyroid veins.

Pressure and flow rate waveforms in systemic veins are shown in figure 23. Blood flow in systemic veins is highly pulsatile, with a biphasic behaviour. By biphasic we mean that, contrary to what happens in arteries, there are two marked peaks in both, pressure and flow. This pulsatility is due to the direct connection of caval veins to the right atrium and the consequent retrograde pressure pulses traveling opposite to blood flow direction [48, 70]. The first flow peak, which is normally the highest one, is due to atria relaxation and consequently filling of this chamber, whereas the second one is related to the opening of the tricuspid valve. Depending on the degree of valvular competence, flow may be retrograde after the second peak. Computed flow waveforms resemble the expected biphasic behaviour and reflect the great influence of the right atrium in systemic venous flow patterns.

In the case of dural sinuses (major intracranial veins) and neck veins, time-resolved PC-MRI flow rate data is available. Computed pressure and flow rate, as well as PC-MRI flow measurements are shown in figures 24 to 26. We note that flow rate measurements correspond to the same patient for which major head and neck veins were characterized. Computed flow rate waveforms well reproduce measured ones, with a biphasic behaviour and the highest peak in correspondence of ventricular systole. There are however expected discrepancies between our computational results and PC-MRI flow data. In particular, there is a mismatch in average flow rate at C5-C6 and C7-T1 levels for the left internal jugular vein (figures 25(l) and 26(f)). This missing mass influences also the matching between time resolved measurements and computational results at those locations. The mass mismatch is due to the fact that cerebral blood flow is not imposed in the model, but is a result of computations. Since we are characterizing only major head and neck veins, while using a *standard* network of arteries, veins and capillary bed, this kind of results is expected.

There are certainly other factors that will influence venous waveforms which were not taken into account in the present model. In the next section we identify these factors and discuss their potential influence.

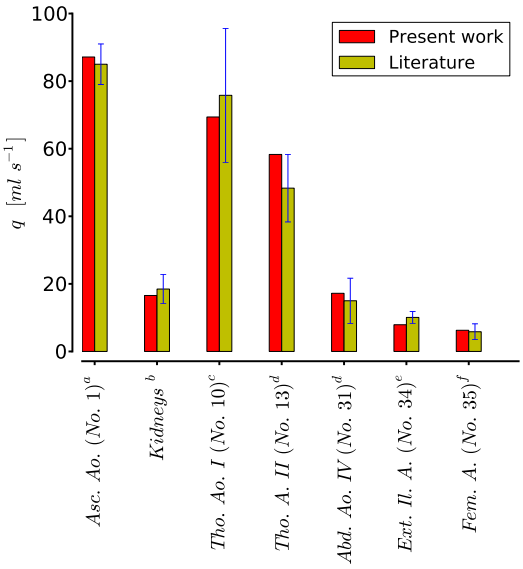

Figure 15: Blood flow distribution along the aorta and major leg arteries: computational results *vs* literature data (average and standard deviation). Asc. Ao.: Ascending Aorta; Kidneys: sum of both Renal Arteries; Tho. Ao.: Thoracic Aorta; Abd. Ao.: Abdominal Aorta; Ext. Il. A.: External Iliac Artery; Fem. A.: Femoral Artery. Vessel numbers refer to table 3 and figure 1. References: [a]Murgo *et al.* [61]; [b]Wolf *et al.* [94]; [c]Zitnik *et al.* [98]; [d]Cheng *et al.* [21]; [e]Itzchak *et al.* [43]; [f]Lewis *et al.* [49].

6 Discussion and future work

Closed-loop models make it possible to study a wide range of physiological and pathological conditions [51, 12], avoiding the imposition of boundary conditions. On the other hand, their construction requires the characterization of a complex multi-scale set of models and their coupling. Therefore, such models have to be thoroughly validated, comparing computational results to physiological realistic situations and, ideally, to measurements. In section 5 we have presented computational results for major compartments described by the proposed model, comparing them to physiological data reported in the literature and to MRI derived flow quantification data. We have seen that heart dynamics are well described, with a correct interaction among heart chambers and between the left ventricle and the ascending aorta. Waveform patterns in the arterial system are in accordance with general physiological data and blood flow distribution among organs is reasonable.

The same conclusions made for the arterial system can be drawn for the venous circulation. The one-dimensional description of the venous district of our model is in fact a novel aspect of the present work. The emphasis given to the venous system in this work can not be found in previous works that presented models with a one-dimensional description of this cardiovascular district [75, 3], even in the context of closed-loop models [90]. Always with regard to the venous system, a distinctive aspect of the present work is represented by the detailed description of head and neck veins, which takes into account collateral pathways for cerebral venous drainage. This choice is motivated by the future applications envisaged in the context of this work with regard to the performance of a computational study of haemodynamical aspects of CCSVI [97].

Our experience, derived from modelling several patients for which MRI-derived geometry and PC-MRI time-resolved flow rate measurements were available, suggests us that a patient-specific characterization of major head and neck veins via medical imaging-derived geometries is necessary to satisfactorily reproduce measurements. In order to illustrate this fact we report a limited number of computational results for a second healthy control. The model is kept as described in section 4, except for some major head and neck veins, which are modified according to patient-specific MRI-derived geometrical information.

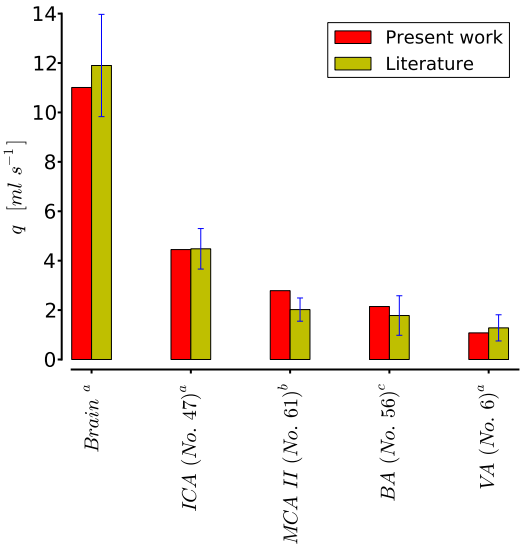

Figure 16: Blood flow in head and neck arteries: computational results *vs* literature data (average and standard deviation). Brain: sum of average flow rate in both internal carotid and vertebral arteries; ICA: Internal Carotid Artery; MCA: Middle Cerebral Artery; BA: Basilar Artery; VA: Vertebral Artery. Vessel numbers refer to table 3 and figure 1. References: [a]Stoquart-ElSankari *et al.* [81]; [b]Stock *et al.* [80]; [c]Boorder *et al.* [14].

Modified vessels are reported in table 11. In figure 27 we compare measured and computed average flow rates at two levels of internal jugular veins (unfortunately no measurement for dural sinuses are available for this patient). We can see that measured average flow at these locations is different from the one previously reported (see figure 22). We can also observe that modifying the venous network in this region is sufficient for obtaining a satisfactory agreement between measured and computed flow distribution. In figure 28 we show time-resolved flow measurements and computed flow rates in two veins. As for the healthy control presented in section 5, also in this case the amplitude of the first peak in the flow rate waveform is satisfactorily reproduced.

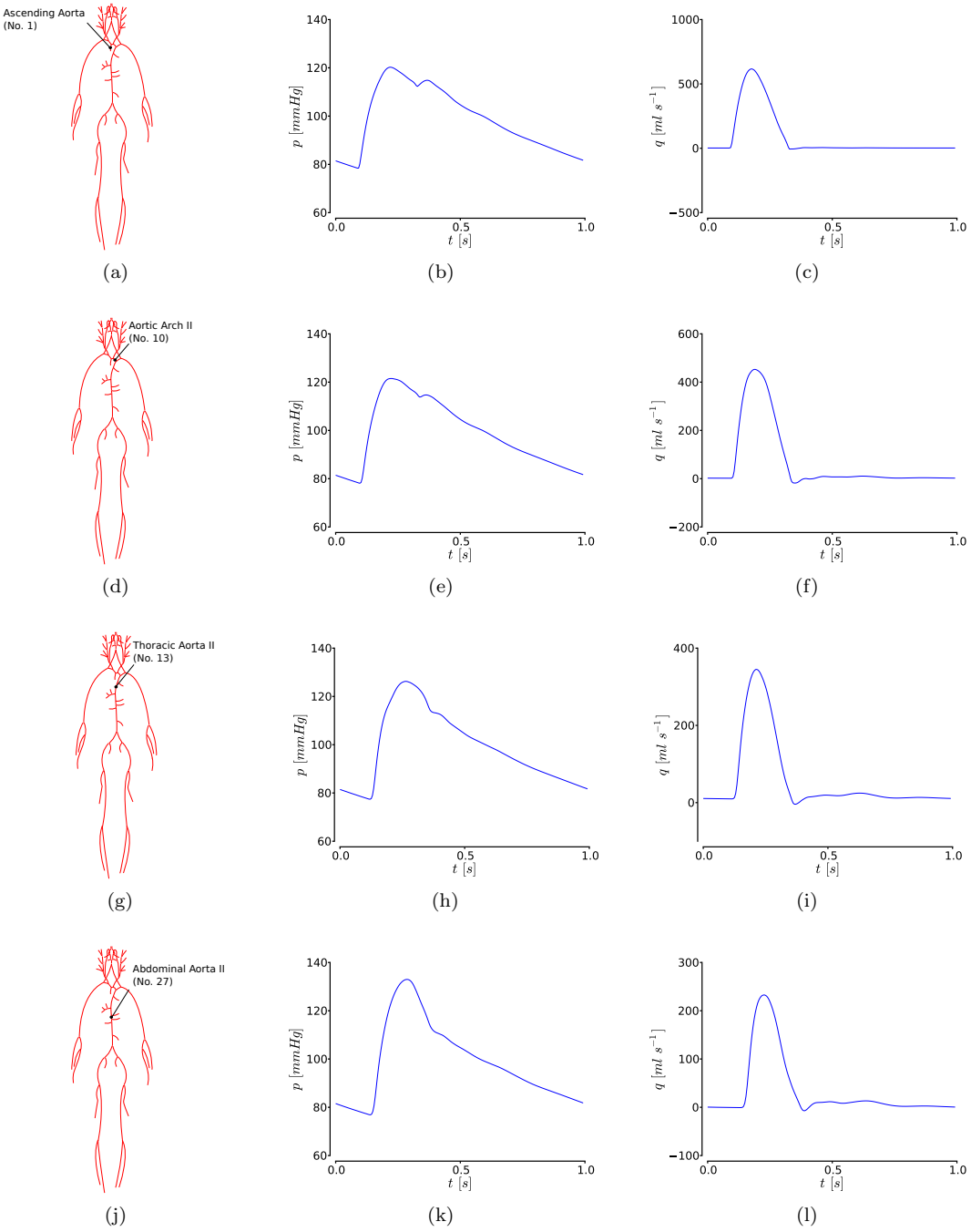

Figure 17: Computed pressure and flow rate along the aorta.

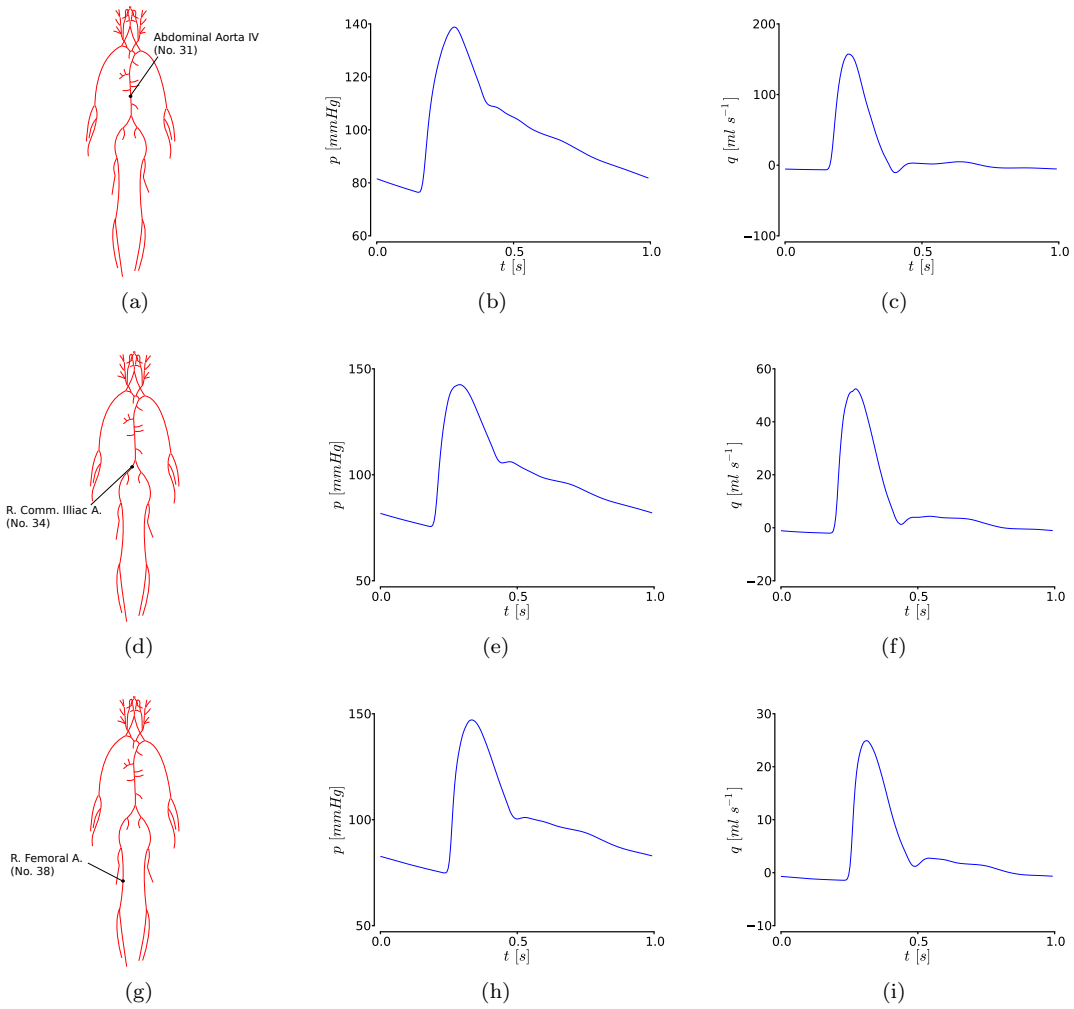

Figure 18: Computed pressure and flow rate in the aorta and major leg arteries.

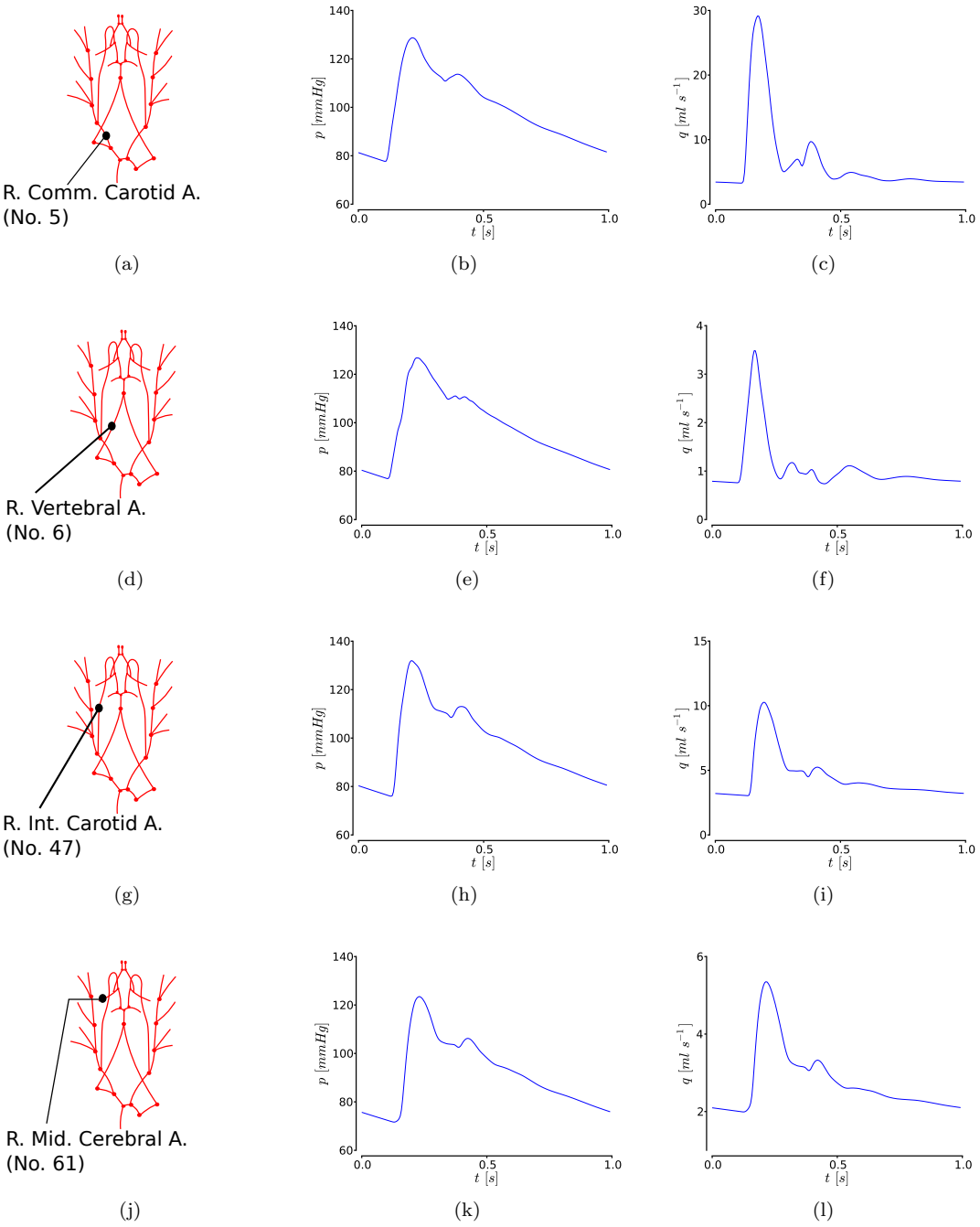

Figure 19: Computed pressure and flow rate in head and neck arteries.

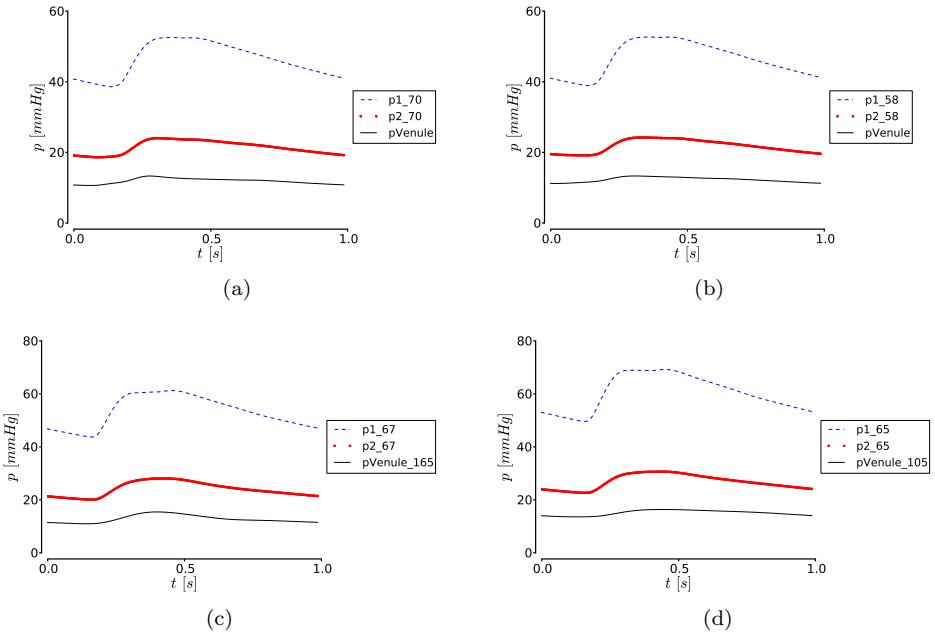

Figure 20: Computed pressure values for arterioles, capillaries and venules for selected elements of lumped compartments E (top left), F (top right) and G (bottom row). $p1$ stands for arterioles, $p2$ for capillaries and $pVenule$ for venules. Numbers correspond to the vessels that are connected to lumped compartment elements.

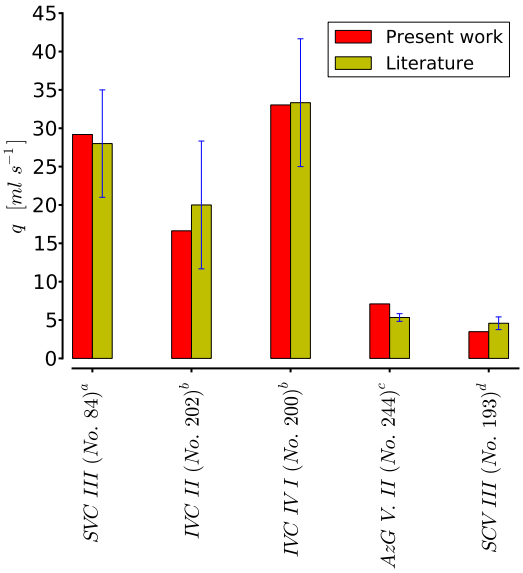

Figure 21: Blood flow in selected systemic veins: computational results *vs* literature data (average and standard deviation). SVC: Superior Vena Cava; IVC: Inferior Vena Cava; AzG V.: Azygos Vein; SCV: Subclavian Vein. Vessel numbers refer to figure 2 and table 8. References: [a] Be'eri *et al.* [11]; [b] Cheng *et al.* [21]; [c] Nabeshima *et al.* [63]; [d] Fortune & Feustel [36].

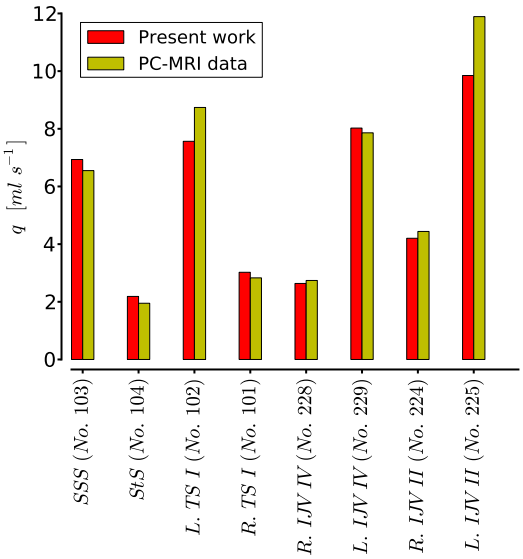

Figure 22: Blood flow in head and neck veins: computational results *vs* MRI flow quantification data. SSS: Superior sagittal Sinus; StS: Straight Sinus; TS: Transverse Sinus; IJV: Internal Jugular Vein. Vessel numbers refer to figure 2 and table 8.

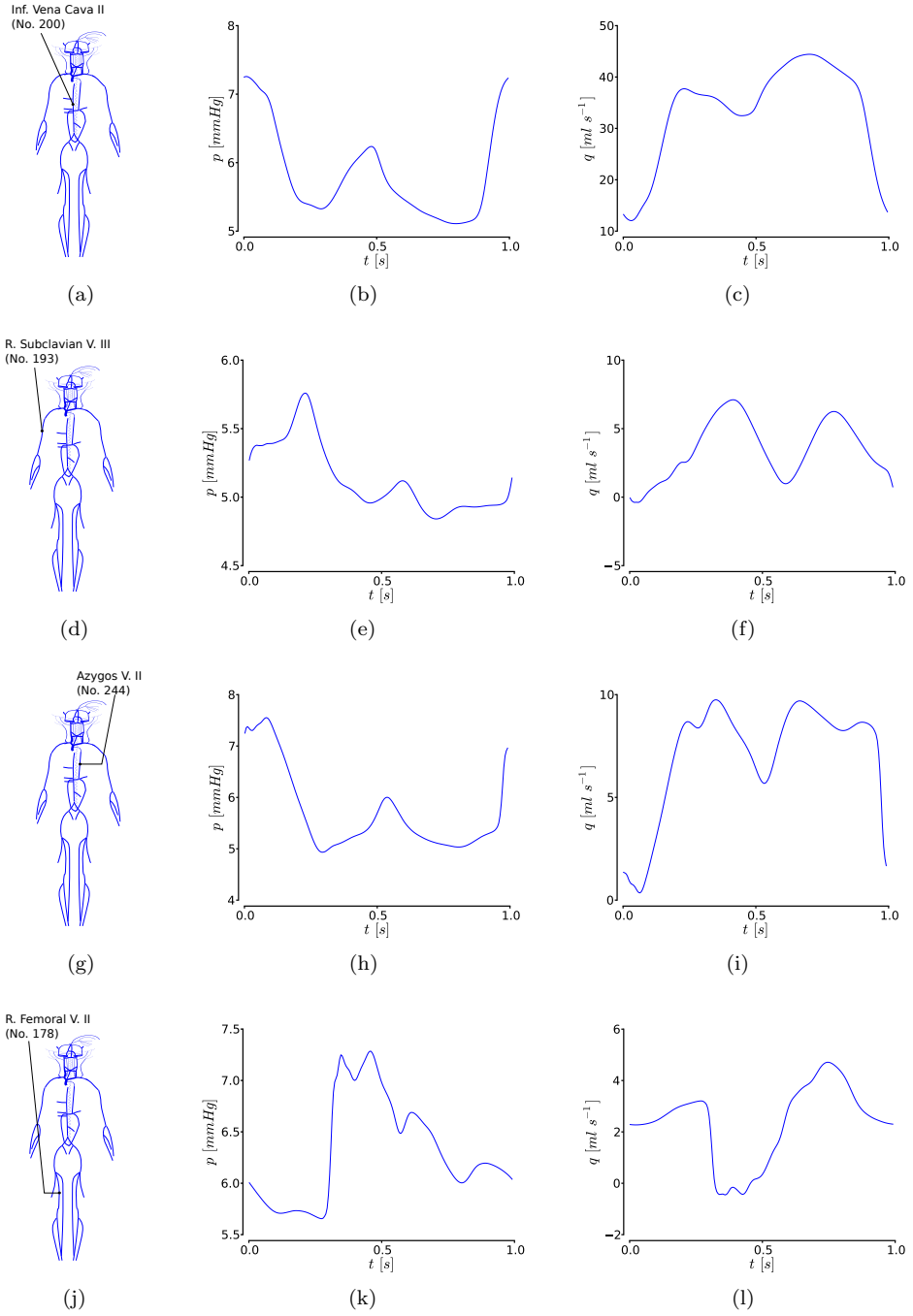

Figure 23: Computed pressure and flow rate in selected systemic veins.

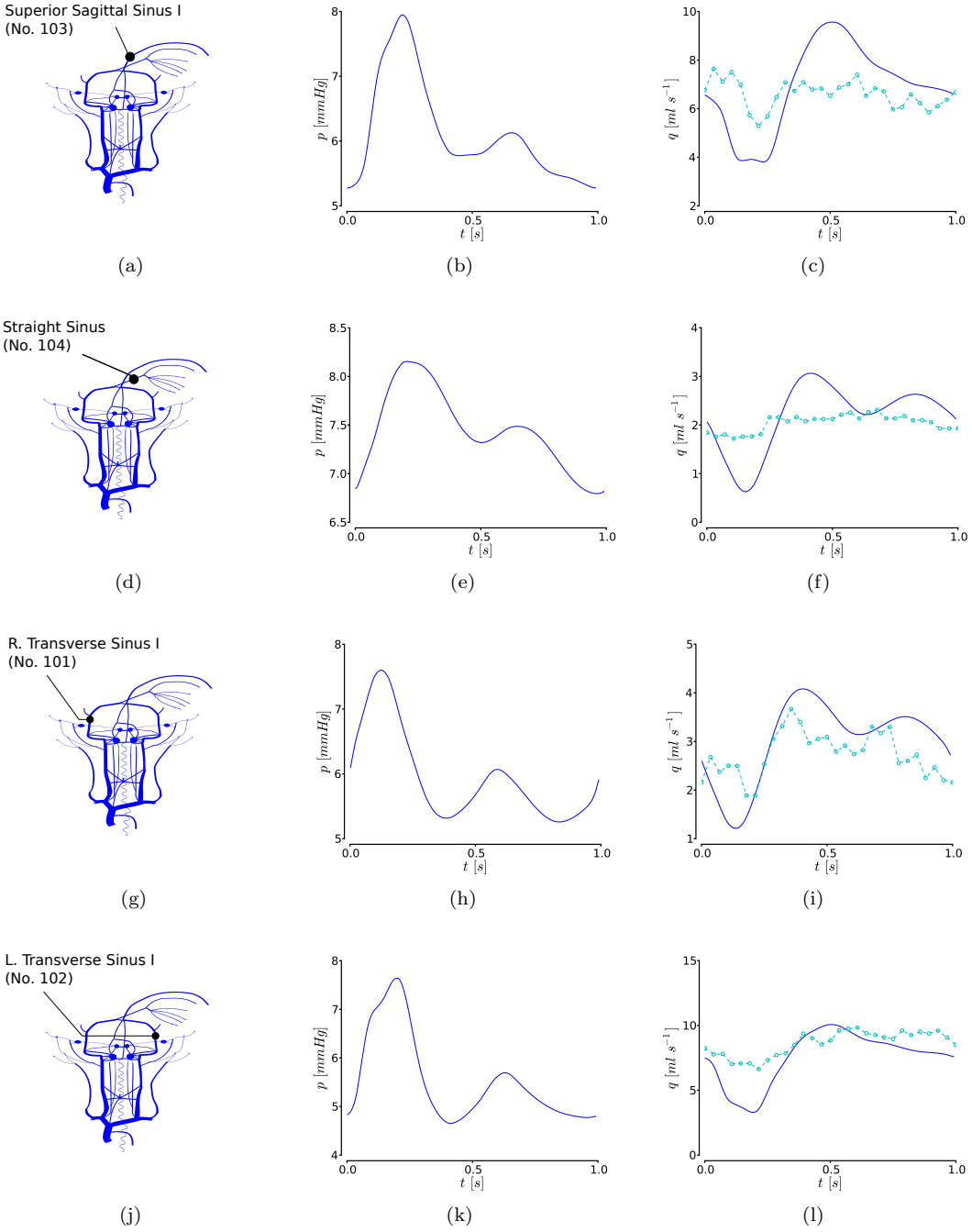

Figure 24: Computed pressure and flow rate in dural sinuses. PC-MRI flow quantification data is shown with symbols and dashed lines.

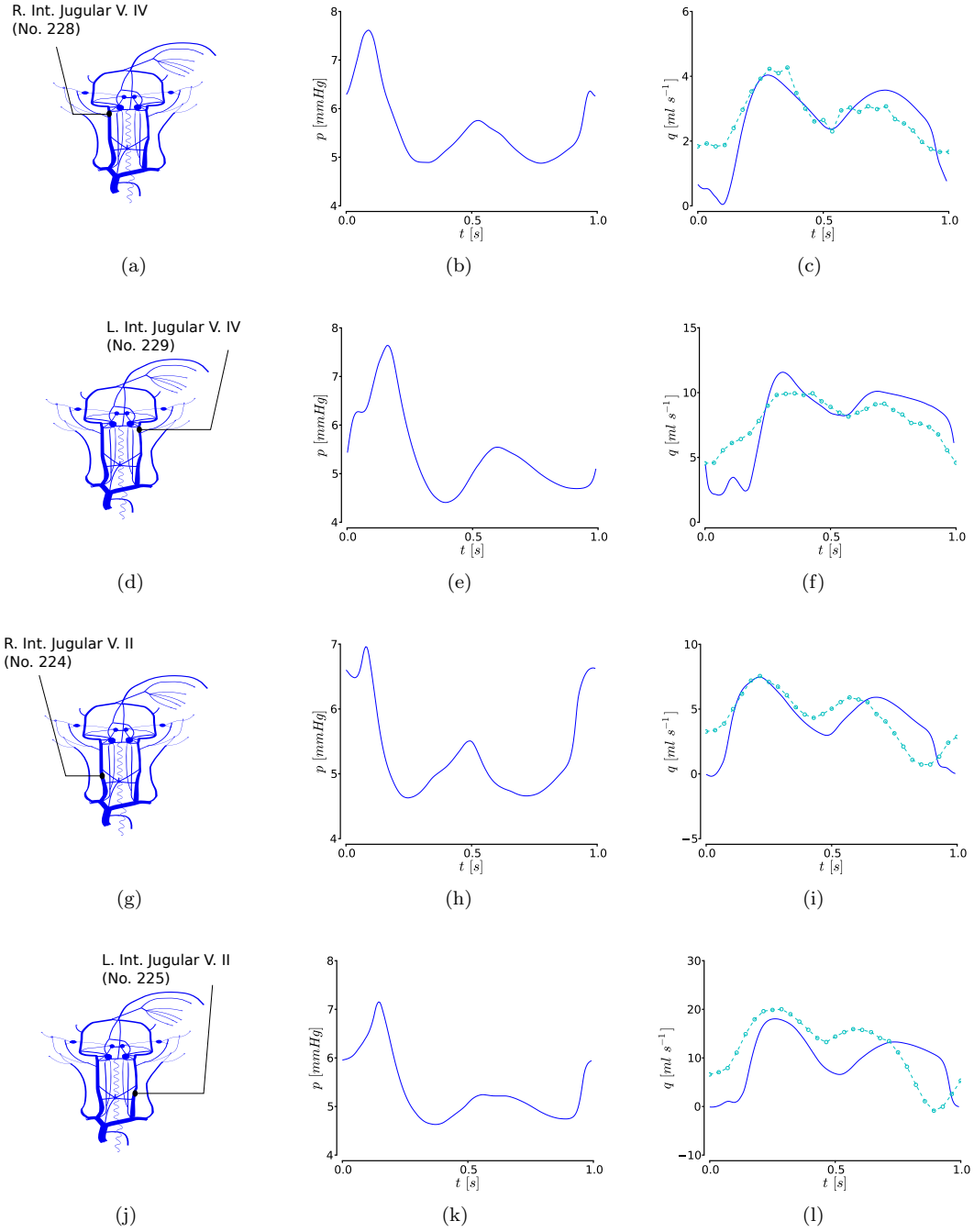

Figure 25: Computed pressure and flow rate in internal jugular veins. PC-MRI flow quantification data is shown with symbols and dashed lines.

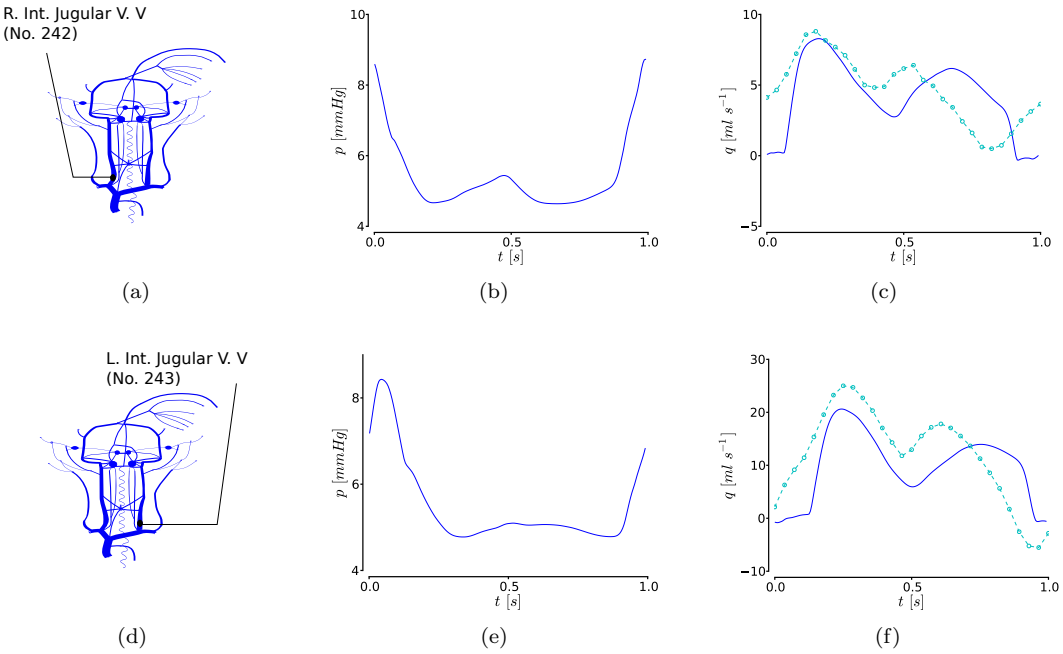

Figure 26: Computed pressure and flow rate in internal jugular veins (cont. from figure 25). PC-MRI flow quantification data is shown with symbols and dashed lines.

Table 11: Geometrical and mechanical parameters for modified head and neck veins of alternative venous network. L: length; r_0: inlet radius; r_1: outlet radius; c_0: wave speed for $A = A_0$; Loc location in the body according to table 2; Ref : MRI imaging derived segmented geometry.

No.	Vessel name	$L\ [cm]$	$r_0\ [cm]$	$r_1\ [cm]$	$c_0\ [m/s]$	Loc.	Ref.
92	R. int. jugular v. I	2.50	0.472	0.505	1.494	3	MRI
99	R. sigmoid sinus II	3.50	0.309	0.252	3.000	1	MRI
101	R. trans. sinus I	3.50	0.219	0.219	3.000	1	MRI
102	L. trans. sinus I	3.50	0.334	0.178	3.000	1	MRI
224	R. int. jugular v. II	3.00	0.437	0.472	1.558	3	MRI
226	R. int. jugular v. III	2.70	0.357	0.437	1.673	3	MRI
227	L. int. jugular v. III	2.70	0.399	0.564	1.506	3	MRI
228	R. int. jugular v. IV	6.80	0.309	0.357	1.814	3	MRI
229	L. int. jugular v. IV	6.80	0.399	0.399	1.669	3	MRI
230	R. sigmoid sinus I	1.50	0.252	0.309	3.000	1	MRI
232	R. trans. sinus II	3.50	0.219	0.309	3.000	1	MRI
233	L. trans. sinus II	3.50	0.178	0.399	3.000	1	MRI
242	R. int. jugular v. V	1.00	0.505	0.505	1.463	3	MRI
259	Confluence of sinuses	1.00	0.219	0.219	3.000	1	MRI

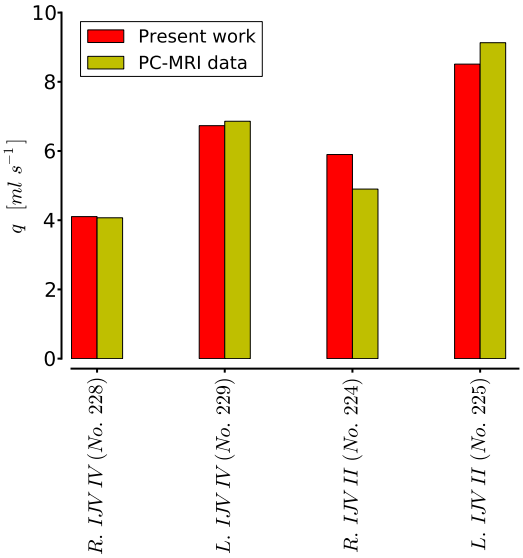

Figure 27: Blood flow in neck veins for a venous network modified according to in table 11: computational results *vs* MRI flow quantification data. IJV: Internal Jugular Vein. Vessel numbers refer to figure 2 and table 11.

Computational results for the venous district show that the non-pulsatile character of venous blood flow is a myth. In fact, we can see how right atrium retrograde pressure waves greatly influence venous flow, creating a biphasic flow pattern. This behaviour is well-known to the medical community and must be reproduced by any model of the venous system [70, 48].

The pulsatility of venous blood flow will be further influenced by factors. The most significant ones are respiration, gravity and venous tone regulation. The satisfactory agreement between computational results and MRI-derived data for a subject at rest in supine position suggests that none of these factors plays a crucial role in the determination of venous flow patterns in body regions where measurements were available. In order to determine the effect of respiration on venous flow pulsatility we have performed a

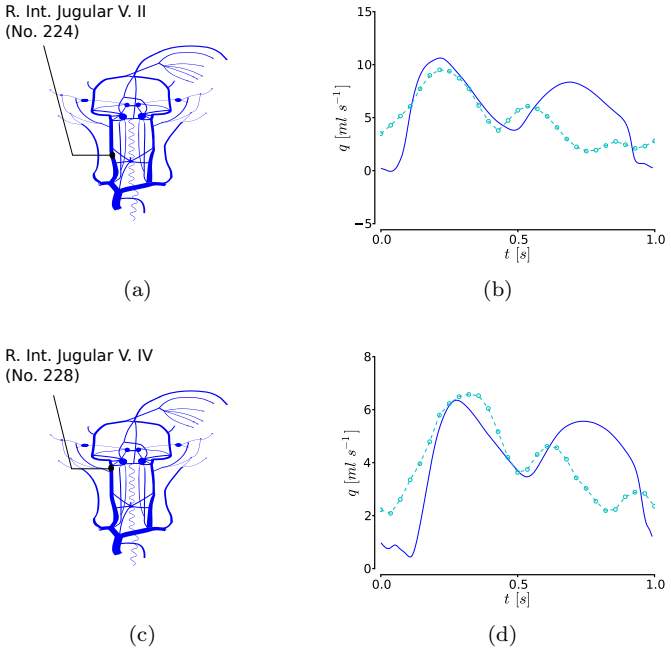

Figure 28: Computed pressure and flow rate in internal jugular veins for a venous network modified according to in table 11 . PC-MRI flow quantification data is shown with symbols and dashed lines.

simulation in which intra-thoracic and intra-abdominal pressures vary, as proposed by [83], according to

$$P_k = \begin{cases} P_{k,a} + P_{k,b} \left(1 - \exp(-\dfrac{\hat{t}}{\tau})\right) & \text{if} \quad \hat{t} \leq t_{insp}\,, \\ P_{k,a} + P_{k,b}\, \exp(-\dfrac{(\hat{t} - t_{insp})}{\tau})) & \text{if} \quad \hat{t} > t_{insp}\,, \end{cases} \quad \text{with} \quad k = th, abd\,, \tag{45}$$

where $\hat{t} = mod(t, t_{resp})$, t_{resp} is the duration of a respiratory cycle, t_{insp} is the duration of the inspiration phase, τ is a decay constant, $P_{k,a}$ and $P_{k,b}$ are the baseline pressure and variation amplitude, respectively. According to [83], the duration of the respiratory cycle is $t_{resp} = 5\,s$, with an inspiration phase of $t_{insp} = 2\,s$ and a decay constant $\tau = 0.3\,s$. Moreover, baseline intra-thoracic pressure is $P_{th,a} = -3.7\,mmHg$ and its variation amplitude is $P_{th,b} = -1.8\,mmHg$. For the intra-abdominal cavity we use the same time coefficients as for the intra-thoracic cavity, while baseline pressure is $P_{ab,a} = 1\,mmHg$ and variation amplitude is $P_{ab,b} = 1.8\,mmHg$, according to [78]. In figure 29 we show computational results for two veins, one located in the neck and the other one in the abdomen, for a period of 10 seconds. It can be clearly seen that while there is a modulation of flow and pressure due to respiration, the shape of pressure and flow waves is chiefly determined by the right heart. However, we expect that in the case of respiratory manoeuvres, such as Valsava and Müller manoeuvres, or other situations such as postural changes and exercise, respiration along with venous tone regulation and muscle compression will play a crucial role in the determination of venous hemodynamics.

The introduction of gravity during postural changes will introduce transient flow acceleration and vessel collapse above the right atrium due to negative transmural pressure [7, 44]. Under these circumstances the wave speed for veins in the collapse region will certainly lead to transcritical flows and therefore will make the algorithm used to treat junctions unsuitable. This fact was confirmed by preliminary numerical experiments that we do not report here. Therefore, it is necessary to introduce new methodologies for the treatment of junctions. This subject is in fact being currently investigated by the authors.

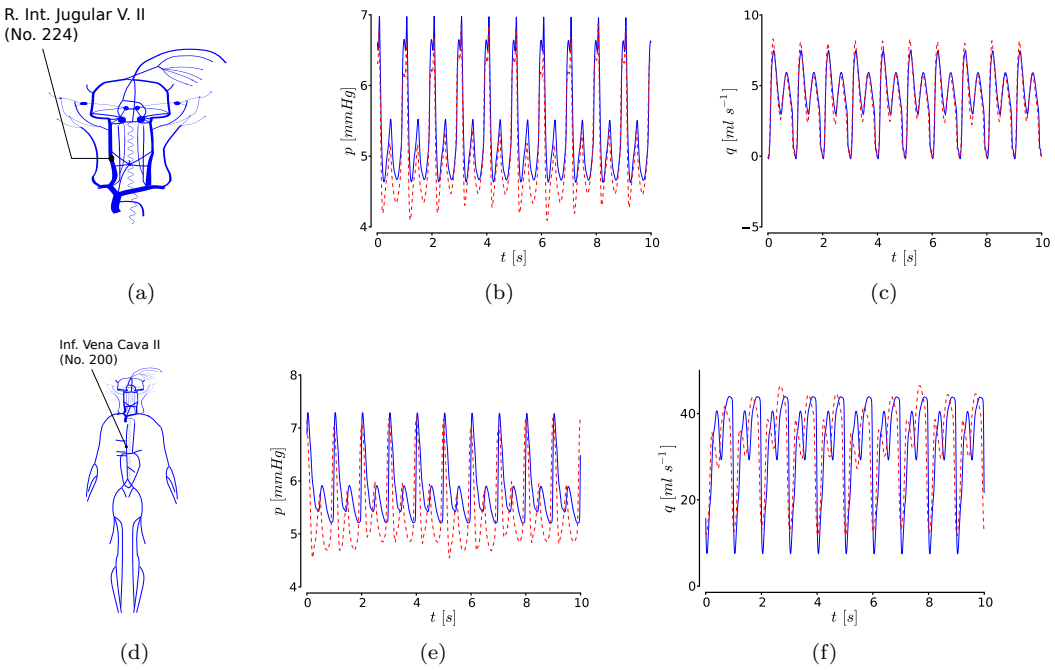

Figure 29: Computed pressure and flow rate for the right internal jugular vein (top row) and the inferior vena cava (bottom row). Continuous lines correspond to results obtained without including respiration and dashed lines represent results obtained including variation of intra-thoracic and intra-abdominal pressures as specified by equation (6).

Venous tone regulation due to postural changes will act simultaneously with blood flow regulation in other compartments, such as arterioles [48]. We plan to include mathematical models of the baroreflex regulatory system, as the one proposed in [13].

A further aspect that will play a crucial role for the correct description of postural changes is the use of a realistic tube law (18). The authors are convinced about the fact that the pressure-area relationship used in this paper has to be improved in order to correctly represent transient phases due to postural changes.

Having always the motivation of this work in mind, another element to be added to the present model is that of the interaction between brain parenchyma, cerebro-spinal flow and cerebral vasculature. Some work attempting to model this complex phenomena is readily available [52] and will be used as a starting point.

7 Summary and concluding remarks

We have presented a closed-loop, multi-scale model comprising lumped-parameter models for the heart, the pulmonary circulation and the microvasculature, together with one-dimensional description of medium to large arteries and veins. A novel feature of the model is the detailed description of the venous system, particularly that part related to the head and neck. This is so because we are chiefly interested in the application of the model to the theoretical study of the connection between the venous vasculature and a class of neurodegenerative diseases. Regarding the lumped-parameter models, their numerical aspects are well researched. However, concerning the one-dimensional models, the hyperbolic character of the governing equations poses significant challenges to the numerical modeller. Particular issues are vessel collapse, choking, elastic jump formation and geometric-type source terms. In this model we have deployed state-of-the-art numerical methodologies that are able to cope with these challenges. These issues are particularly relevant to the modelling of the venous system, which is significantly more challenging than the well-researched arterial system. A systematic assessment and validation exercise has been carried out, making abundant use of published results, as well as recent measurements of flow in head and neck veins, kindly provided to us by our collaborators. For this portion of the domain we have performed a patient-specific characterisation of major vessels. We have shown that this step is necessary in order to correctly reproduce PC-MRI derived flow patterns in a patient-specific manner. We have also discussed some potential improvements to the model in order to correctly describe postural changes, which will be the subject of a forthcoming publication.

Acknowledgements

The authors warmly thank Prof. E. M. Haacke (MR Research Facility, Wayne State University, Detroit, USA) for providing MRI data used in this work. This work has been partially funded by CARITRO (*Fondazione Cassa di Risparmio di Trento e Rovereto*, Italy), project No. 2011.0214.

References

[1] J. Alastruey, A. W. Khir, K. S. Matthys, P. Segers, and S. J. Sherwin. Pulse wave propagation in a model human arterial network: Assessment of 1-D visco-elastic simulations against *in vitro* measurements. *Journal of Biomechanics*, 44:2250–2258, 2011.

[2] J. Alastruey, K. H. Parker, J. Peiró, and S. J. Sherwin. Lumped parameter outflow models for 1-D blood flow simulations: Effect on pulse waves and parameter estimation. *Communications in Computational Physics*, 4:317–336, 2008.

[3] M. T. Alirezaye-Davatgar. *Numerical Simulation of Blood Flow in the Systemic Vasculature Incorporating Gravitational Force with Application to Cerebral Circulation.* PhD thesis, Graduate School of Biomedical Engineering - University of New South Wales, 2006.

[4] M. Anliker, M. K. Wells, and E. Ogden. The transmission characteristics of large and small pressure waves in the abdominal vena cava. *IEEE Transactions on Bio-Medical Engineering*, 16:262–273, 1969.

[5] L. Antiga, M. Piccinelli, L. Boti, B. Ene-Iordache, A. Remuzzi, and D. A. Steinmann. An image-based modeling framework for patient-specific computational hemodynamics. *Medical and Biological Engineering and Computing*, 46:1097–1112, 2008.

[6] K. I. Arnautovic, O. Al-Metfy, T. Glenn, A. F. Krisht, and M. M. Husain. The suboccipital cavernous sinus. *Journal of Neurosurgery*, 86:252–262, 1997.

[7] P. Avasthey. Venous pressure changes during orthostasis. *Cardiovascular Research*, 6:657–663, 1972.

[8] A. P. Avolio. Multi-branched model of the human arterial system. *Medical and Biological Engineering and Computing*, 18:709–718, 1980.

[9] N. Balak, G. Ersoy, U. Uslu, N. Tanriöver, L. Tapul, G. Cetin, N. Isik, and I. Elmaci. Microsurgical and histomorphometric study of the occipital sinus: Quantitative measurements using a novel approach of stereology. *Clinical Anatomy*, 23:386–393, 2010.

[10] S. Bassez, P. Flaud, and M. Chauveau. Modeling of the Deformation of Flexible Tubes Using a Single Law: Application to Veins of the Lower Limb in Man. *Journal of Biomechanical Engineering*, 123:58–65, 2001.

[11] Eliezer Beeri, Stephan E. Maier, Michael J. Landzberg, Taylor Chung, and Tal Geva. In vivo evaluation of fontan pathway flow dynamics by multidimensional phase-velocity magnetic resonance imaging. *Circulation*, 98(25):2873–2882, 1998.

[12] P. J. Blanco, M. R. Pivello, S. A. Urquiza, and R. A. Feijóo. On the potentialities of 3D-1D coupled models in hemodynamics simulations. *Journal of Biomechanics*, 42:919–930, 2009.

[13] P. J. Blanco, P. R. Trenhago, L. G. Fernandes, and R. A. Feijóo. On the integration of the baroreflex control mechanism in a heterogeneous model of the cardiovascular system. *International Journal for Numerical Methods in Biomedical Engineering*, 28(4):412–433, 2012.

[14] M. J. Boorder, J. Hendrikse, and J. ven der Grond. Phase-contrast magnetic resonance imaging measurements of cerebral autoregulation with a breath-hold challenge: A feasibility study. *Stroke*, 35:1350–1354, 2004.

[15] B. S. Brook, S. A. E. G. Falle, and T. J. Pedley. Numerical solutions for unsteady gravity-driven flows in collapsible tubes: evolution and roll-wave instability of a steady state. *Journal of Fluid Mechanics*, 396:223–256, 1999.

[16] B. S. Brook and T. J. Pedley. A model for time-dependent flow in (giraffe jugular) veins: uniform tube properties. *Journal of Biomechanics*, 35:95–107, 2002.

[17] R. W. Brower, R. R. Reddy, and A. Noordergraaf. Difficulties in the further development of venous hemodynamics. *IEEE Transactions on Bio-Medical Engineering*, 16:335–338, 1969.

[18] C. G. Caro, T. J. Pedley, R. C. Schroter, and W. A. Seed. *The Mechanics of the Circulation*. Cambridge University Press, second edition, 2012.

[19] R. D. Caruso, A. E. Rosenbaum, J. K. Chang, and S. E. Joy. Craniocervical junction venous anatomy on enhanced MR images: The suboccipital cavernous sinus. *American Journal of Neuroradiology*, 20:1127–1131, 1999.

[20] Vincenzo Casulli, Michael Dumbser, and Eleuterio F. Toro. Semi-implicit numerical modeling of axially symmetric flows in compliant arterial systems. *International Journal for Numerical Methods in Biomedical Engineering*, 28(2):257–272, 2012.

[21] C. P. Cheng, R. J. Herfkens, and C. A. Taylor. Inferior vena caval hemodynamics quantified in vivo at rest and during cycling exercise using magnetic resonance imaging. *American Journal of Physiology: Heart and Circulatory Physiology*, 284:H1161–H1167, 2002.

[22] S. Cirovic, C. Walsh, and W. D. Fraser. A Model of Cerebral Blood Flow During Sustained Acceleration. Technical Report DCIEM-98-P-88, Defence and Civil Inst of Environmental Medicine, Downsview ONT (CAN), 1999.

[23] G. Dal Maso, P. G. LeFloch, and F. Murat. Definition and weak stability of nonconservative products. *Journal de Mathématiques Pures et Appliquées*, 74:483–548, 1995.

[24] K. Das, S. A. Begum, S. Dey, M. A. Quddus, and A. S. Mohiuddin. Sonographic measurement of inferior vena cava diameter - a noninvasive tool to detect acute blood loss. *Ibrahim Medical College Journal*, 5, 2011.

[25] T. S. Desser, D. Y. Sze, and R. B. Jeffrey. Imaging and intervention in the hepatic veins. *American Journal of Roentgenology*, 180:1583, 2003.

[26] G. Drzawiecki, S. Field, I. Moubarak, and J. Li. Vessel growth and collapsible pressure area relationship. *American Journal of Physiology - Heart and Circulatory Physiology*, 273:H2030–H2043, 1997.

[27] M. Dumbser, M. Castro, C. Parés, and Toro. ADER schemes on unstructured meshes for nonconservative hyperbolic systems: Applications to geophysical flows. *Computers & Fliuds*, 38:1731–1748, 2009.

[28] M. Dumbser, C. Enaux, and E. F. Toro. Finite volume schemes of very high order of accuracy for stiff hyperbolic balance laws. *Journal of Computational Physics*, 227:3971–4001, 2008.

[29] M. Dumbser, A. Hidalgo, M. Castro, C. Parés, and E. F. Toro. FORCE schemes on unstructured meshes II: Non-conservative hyperbolic systems. *Computational Methods in Applied Mechanics and Engineering*, 199:625–647, 2010.

[30] M. Dumbser and E. F. Toro. On Universal Osher-Type Schemes for General Nonlinear Hyperbolic Conservation Laws. *Communications in Computational Physics*, 10:635–671, 2011.

[31] M. Dumbser and E. F. Toro. A Simple Extension of the Osher Riemann Solver to Non-conservative Hyperbolic Systems. *Journal of Scientific Computing*, 48:70–88, 2011.

[32] D. Elad, R. D. Kamm, and A. H. Shapiro. Choking Phenomena in a Lung-Like Model. *Journal of Biomechanical Engineering*, 109:1–9, 1987.

[33] W. Feng, D. Utriainen, G. Trifan, S. Elias, S. S. Sethi, J. Hewett, and E. M. Haacke. Characteristics of flow through the internal jugular veins at cervical C2/C3 and C5/C6 levels for multiple sclerosis patients using MR phase contrast imaging. *Neurological Research*, 34:802–9, 2012.

[34] J. E. Flaherty, J. B. Keller, and S. I. Rubinow. Post buckling behavior of elastic tubes and rings with opposite sides in contact. *SIAM Journal on Applied Mathematics*, 23:446–455, 1972.

[35] L. Formaggia, A. Quarteroni, and A. Veneziani. *Cardiovascular Mathematics: Modeling and simulation of the circulatory system.* Springer-Verlag Italia, Milano, 2009.

[36] J. B. Fortune and P. Feustel. Effect of patient position on size and location of the subclavian vein for percutaneous puncture. *Archives of Surgery*, 138:996–1000, 2003.

[37] J. Fullana and S. Zaleski. A branched one-dimensional model of vessel networks. *Journal of Fluid Mechanics*, 621:183–204, 2009.

[38] M. N. Gwilliam, N. Hoggard, D. Capener, P. Singh, A. Marzo, P. K. Verma, and I. D. Wilkinson. MR derived volumetric flow rate waveforms at locations within the common carotid, internal carotid, and basilar arteries. *Journal of Cerebral Blood Flow & Metabolism*, 29:1975–1982, 2009.

[39] E. M. Haacke, C. Beggs, and C. Habib. The role of venous abnormalities in neurological disease. *Reviews on Recent Clinical Trials*, 7:100–116, 2012.

[40] E. M. Haacke, M. Liu, and H. Xu. Investigating venous abnormaities and white matter hypersensitivities in idiopathic parkinsons disease using magnetic resonance imaging. 2013. submitted.

[41] B. S. Hertzber, M. A. Kliewer, D. M. DeLong, K. J. Lalouche, E. K. Paulson, M. G. Frederick, and B. A. Carroll. Sonographic assessment of lower limb vein diameters: Implcations for the diagnosis and characterization of deep venous thrombosis. *American Journal of Radiology*, 168:1253–1257, 1997.

[42] H. Ho, K. Mithraratne, and P. Hunter. Numerical simulation of blood flow in an anatomically-accurate cerebral venous tree. *IEEE Transactions on Medical Ima*, 2012.

[43] Y. Itzchak, M. Modan, R. Adar, and V. Deutsch. External iliac artery blood flow in patients with arteriosclerosis obliterans. *American Journal of Roentgenology*, 125:437–441, 1975.

[44] T. Iwabuche, E. Sobata, K. Ebina, H. Tsubakisaka, and M. Takiguchi. Dural sinus pressure: various aspects in human brain surgery in children and adults. *American Journal of Physiology - Heart and Circulatory Physiology*, pages H389–H396, 1986.

[45] R. D. Kamm and A. H. Shapiro. Unsteady flow in a collapsible tube subjected to external pressure or body forces. *Journal of Fluid Mechanics*, 95:1–78, 1979.

[46] R. Kölegard, I. B. Mekjavic, and O. Eiken. Increased distensibility in dependent veins following prolonged bedrest. *European Journal of Applied Physiology*, 106:547–554, 2009.

[47] T. Kutoglu, M. Turut, N. Kocabiyik, H. Ozan, and M. Yildrim. Anatomical analysis of azygos vein system in human cadavers. *Romanian Journal of Morphology & Embryology*, 53:1051–1056, 2012.

[48] J. R. Levick. *An introduction to cardiovascular physiology.* Hodder Arnold, 2010.

[49] P. Lewis, Psaila J. V., Davies W. T., K. McCarty, and J.P. Woodcock. Measurement of volume flow in the human common femoral artery using a duplex ultrasound system. *Ultrasound in Medicine and Biology*, 10:777–784, 1986.

[50] F. Y. Liang, K. Fukasaku, H. Liu, and S. Takagi. A computational model study of the influence of the anatomy of the circle of Willis on cerebral hyperperfusion following carotid artery surgery. *Biomedical Engineering Online*, 10, 2011.

[51] F. Y. Liang, S. Takagi, R. Himeno, and H. Liu. Biomechanical characterization of ventricular-arterial coupling during aging: A multi-scale model study. *Journal of Biomechanics*, 42:692–704, 2009.

[52] A. A. Linninger, M. Xenos, B. Sweetman, S. Ponkshe, X. Guo, and R. Penn. A mathematical model of blood, cerebrospinal fluid and brain dynamics. *Journal of Mathematical Biology*, 59:729–759, 2009.

[53] R. G. Louis, M. Loukas, C. T. Wartmann, R. S. Tubbs, N. Apaydin, A. A. Gupta, G. Spentzouris, and J. R. Ysique. Clinical anatomy of the mastoid and occipital emissary veins in a large series. *Surgical Radiologic Anatomy*, 31:139–144, 2009.

[54] E. Marchandise and P. Flaud. Accurate modelling of unsteady flows in collapsible tubes. *Computer Methods in Biomechanics and Biomedical Engineering*, 13:279–290, 2010.

[55] G. I. Montecinos, C. E. Castro, M. Dumbser, and E. F. Toro. Comparison of solvers for the generalized Riemann problem for hyperbolic systems with source terms. *Journal of Computational Physics*, 231:6472–6494, 2012.

[56] A. H. Moreno, A. I. Katz, and L. D. Gold. An integrated approach to the study of the venous system with steps towards a detailed model of the dynamics of venous return to the right heart. *IEEE Transactions on Bio-Medical Engineering*, 16:308–324, 1969.

[57] L. O. Müller, Montecinos G. I., and E. F. Toro. Some issues in modelling venous haemodynamics. In P. García-Navarro M. E. Vázquez-Cendón, A. Hidalgo and L. Cea (editors), editors, *Numerical Methods for Hyperbolic Equations: Theory and Applications. An international conference to honour Professor E. F. Toro*, pages 347–354. CRC Press, Taylor & Francis Group, 2013.

[58] Lucas O. Müller, Carlos Parés, and Eleuterio F. Toro. Well-balanced high-order numerical schemes for one-dimensional blood flow in vessels with varying mechanical properties. *Journal of Computational Physics*, 242:53 – 85, 2013.

[59] Lucas O. Müller and Eleuterio F. Toro. Well-balanced high-order solver for blood flow in networks of vessels with variable properties. *International Journal for Numerical Methods in Biomedical Engineering*, 2013.

[60] M. L. Munoz-Ruiz and C. Parés. On the Convergence and Well-Balanced Property of Path-Conservative Numerical Schemes for Systems of Balance Laws. *Journal of Scientific Computing*, 48:274–295, 2011.

[61] J P Murgo, N Westerhof, J P Giolma, and S A Altobelli. Aortic input impedance in normal man: relationship to pressure wave forms. *Circulation*, 62(1):105–16, 1980.

[62] J. P. Mynard. *Computer modelling and wave intensity analysis of perinatal cardiovascular function and dysfunction*. PhD thesis, Department of Paedriatics, The University of Melbourne, 2011.

[63] M. Nabeshima, F. Moriyasu, K. Nishikawa, N. Hamato, M. Fujimoto, and T. Nada. Azygos venous blood flow: measurement with direct bolus imaging. *Radiology*, 195:467–470, 1995.

[64] J. H. Nippa, R. H. Alexander, and R. Folse. Pulse wave velocity in human veins. *Journal of Applied Physiology*, 30:558–563, 1971.

[65] A. Noordergraaf and E. Kresch. Introduction. *IEEE Transactions on Bio-Medical Engineering*, 16:235, 1969.

[66] L. Oguzkurt, F. Tercan, M. A. Pourbagher, O. Kizilkilic, R. Turkoz, and F. Boyvat. Computed tomography findings in 10 cases of iliac vein compression (May-Thurner) syndrome. *Europen Journal of Radiology*, 55:421–245, 2005.

[67] S. Osher and F. Solomon. Upwind difference schemes for hyperbolic systems of conservation laws. *Mathematcs of Computation*, 38:339–374, 1982.

[68] C. Parés. Numerical methods for nonconservative hyperbolic systems: a theoretical framework. *SIAM Journal on Numerical Analysis*, 44:300–321, 2006.

[69] C. Parés and M. Castro. On the well-balance property of roe's method for nonconservativehyperbolic systems. applications to shallow-water systems. *ESAIM: Mathematical Modelling and Numerical Analysis*, 38:821–852, 2004.

[70] M. C. Patel, L. H. Berman, H. A. Moss, and S. J. McPherson. Subclavian and internal jugular veins at doppler us: Abnormal cardiac pulsatility and respiratory phasicity as a predictor of complete central occlusion. *Radiology*, 211(2):579–583, 1999.

[71] T. J. Pedley, B. S. Brook, and R. S. Seymour. Blood pressure and flow rate in the giraffe jugular vein. *Philosophical Transactions: Biological Sciences*, 351:855–866, 1996.

[72] P. Reymond, F. Merenda, F. Perren, D. Rüfenacht, and N. Stergiopulos. Validation of a one-dimensional model of the systemic arterial tree. *American Journal of Physiology - Heart and Circulatory Physiology*, 297:H208–H222, 2009.

[73] B. Schaller. Physiology of cerebral venous blood flow: from experimental data in animals to normal function in humans. *Brain Research Reviews*, 46:243–260, 2004.

[74] A. H. Shapiro. Steady flow in collapsible tubes. *Journal of Biomechanical Engineering*, 99:126–147, 1977.

[75] C. Sheng, S. N. Sarwal, K. C. Watts, and A. E. Marble. Computational simulation of blood flow in human systemic circulation incorporating an external force field. *Medical and Biological Engineering and Computing*, 33, 1995.

[76] S. J. Sherwin, V. Franke, J. Peiró, and K. H. Parker. One-dimensional modelling of a vascular network in space-time variables. *Journal of Engineering Mathematics*, 47:217–250, 2003.

[77] A. Siviglia and Toffolon. M. Steady analysis of transcritical flows in collapsible tubes with discontinuous mechanical properties: implications for arteries and veins. *Journal of Fluid Mechanics*, 2013. In Press.

[78] M. F. Snyder and V. C. Rideout. Computer simulation studies of the venous circulation. *IEEE Transactions on Bio-Medical Engineering*, 16:325–334, 1969.

[79] S. Standring. *Gray's anatomy: the anatomical basis of clinical practice*. Gray's Anatomy: The Anatomical Basis of Clinical Practice. Churchill Livingstone/Elsevier, 2008.

[80] K. W. Stock, S. G. Wetzel, P. A. Lyrer, and E. W. Rad. Quantification of blood flow in the middle cerebral artery with phase-contrast mr imaging. *European Radiology*, 10(11):1795–1800, 2000.

[81] S. Stoquart-ElSankari, P. Lehmann, A. Villette, M. Czosnyka, M. Meyer, H. Deramond, and O. Baledent. A phase-contrast MRI study of physiologic cerebral venous flow. *Journal of Cerebral Blood Flow & Metabolism*, 29:1208–1215, 2009.

[82] M. D. Stringer, M. Restieaux, A. L. Fisher, and B. Crosado. The vertebral venous plexuses: The internal veins are muscular and external veins have valves. *Clinical Anatomy*, 25:609–618, 2012.

[83] Y. Sun, M. Beshara, R. J. Lucariello, and S. A. Chiaramida. A comprehensive model for right-left heart interaction under the influence of pericardium and baroreflex. *American Journal of Physiology*, 272:H1499–515, 1997.

[84] S. Tanoue, H. Kiyosue, M. Okahara, Y. Sagara, Y. Hori, J. Kashiwagi, and H. Mori. Para-cavernous sinus venous structures: Anatomic variations and pathologic conditions evaluated on fat-suppressed 3D fast gradient-echo MR images. *American Journal of Neuroradiology*, 27:1083–1089, 2006.

[85] E. F. Toro, R. Millington, and L. Nejad. Towards very high order godunov schemes. In E. F. Toro, editor, *Godunov Methods. Theory and Applications*, volume 1, pages 897–902. Kluwer/Plenum Academic Publishers, New York, Boston and London, 2001. Conference in Honour of S K Godunov.

[86] E. F. Toro and A. Siviglia. Flow in collapsible tubes with discontinuous mechanical properties: mathematical model and exact solutions. *Communications in Computational Physics*, 13(2):361–385, 2013.

[87] E. F. Toro and V. A. Titarev. Solution of the generalized riemann problem for advection-reaction equations. *Proceedings of the Royal Society A*, 458:271–281, 2002.

[88] E.F. Toro. *Riemann Solvers and Numerical Methods for Fluid Dynamics: A Practical Introduction*. Springer-Verlag, third edition, 2009. ISBN 978-3-540-25202-3.

[89] D. Utriainen, W. Feng, S. Elias, Z. Latif, D. Hubbard, and E. M. Haacke. Using magnetic resonance imaging as a means to study chronic cerebral spinal venous insufficiency in multiple sclerosis patients. *Techniques in Vascular and Interventional Radiology*, 15:101–112, 2012.

[90] Y. V. Vassilevski, S. S. Simakov, and S. A. Kapranov. A multi-model approach to intravenous filter optimization. *International Journal for Numerical Methods in Biomedical Engineering*, 26(7):915–925, 2010.

[91] N. Wafae, K. Hirose, C. Franco, G. C. Wafae, C. R: Ruiz, L. Daher, and O. C. Person. The anatomy of the human thyroid veins and its surgical application. *Folia Morphologica*, 67:221–225, 2008.

[92] L. Wei-hua, W. Shao-ping, and L. Xin. Anatomical observation of the retromandibular vein by mandibular angle ostectomy. *Journal of Clinical Rehabilitative Tissue Engineering Research*, 14:9113–9117, 2010.

[93] J. D. Werner, G. P. Siskin, K. Mandato, M. Englander, and A. Herr. Review of venous anatomy for venographic interpretation in chronic cerebrospinal venous insufficiency. *Journal of Vascular and Interventional Radiology*, 22:1681–1690, 2011.

[94] R. L. Wolf, B. F. King, V. E. Torres, D. M. Wilson, and R. L. Ehman. Measurement of normal renal artery blood flow: cine phase-contrast mr imaging vs clearance of p-aminohippurate. *American Journal of Roentgenology*, 161:995–1002, 1993.

[95] H. Zachrisson, M. Lindenberger, D. Hallman, M. Ekman, D. Neider, and T. Länne. Diameter and compliance of the greater saphenous vein - effect of age and nitroglicerine. *Clinical Physiology and Functional Imaging*, 31:300–306, 2011.

[96] M. Zagzoule and J. P. Marc-Vergnes. A global mathematical model of the cerebral circulation in man. *Journal of Biomechanics*, 19:1015–1022, 1986.

[97] P. Zamboni, R. Galeotti, E. Menegatti, A. M. Malagoni, G. Tacconi, S. Dall'Ara, I. Bartolomei, and F. Salvi. Chronic cerebrospinal venous insufficiency in patients with multiple sclerosis. *Journal of Neurology, Neurosurgery and Psychiatry*, 80:392–399, 2009.

[98] R. S. Zitnik, F. S. Rodich, Hiram W. Marshall, and E. H. Wood. Continuously recorded changes of thoracic aortic blood flow in man in response to leg exercise in supine position. *Circulation Research*, 17(2):97–105, 1965.